The solubility of ITO nanoparticles in this water/hexane mixture phase remains lower than in pure water, and therefore, small ITO nuclei form at an extremely high reaction rate owing to the high degree of supersaturation. The large surface energy of the nanoparticles makes them unstable, causing them to form large aggregations in the absence of an organic modifier. When the fabrication was repeated in the presence of hexanoic acid, the organic ligand capped the nanoparticle surface immediately and limited their growth and tendency for aggregation. As was reported in the previous research,[21,22] strong binding reaction occurs on the surface, which was confirmed by the TGA analysis. As a result, the particle size was controlled. The hydrophobic nature of the surface modifier allows excellent dispersion of the nanoparticles in organic solvent.

The electric resistance of ITO nanoparticles was measured isothermally at room temperature using the four-probe method. To initiate close interparticle contacts, the nanoparticles were pressed to form transparent thin pellets. The conductivity, calculated from electric resistance, is shown in Figure 6. Electric

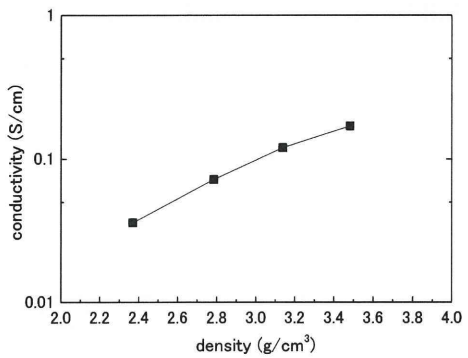

Figure 6. Change in conductivity of modified ITO.

conductivity increases gradually with increasing pressure. At a pressure of 9.6 MPa, a sheet conductivity of 1.2×10^{-1} (S/cm) was measured. This value is roughly the same as for other colloidal ITO particles reported previously, although these nanoparticles are much smaller and display better dispersibility in organic solvent.

CONCLUSIONS

We report a simple and rapid synthetic process for preparing ITO nanoparticles with simultaneous surface modification with an organic ligand by SCFRS. The surface modified particles are highly crystalline ITO nanocrystals with excellent dispersion in organic solvent. Aggregation and crystal growth were effectively suppressed by organic ligand capping. We can get 1–10 g/h under this supercritical condition.

ASSOCIATED CONTENT

Supporting Information

Table of change in peak positions for ITO compared to purdue In_2O_3. This material is available free of charge via the Internet at http://pubs.acs.org.

AUTHOR INFORMATION

Corresponding Author

*Tel & Fax: 81-22-217-6321. E-mail: ajiri@tagen.tohoku.ac.jp.

REFERENCES

(1) Hamberg, I.; Granqivst, C. G. *J. Appl. Phys.* **1986**, *60*, R123–R159.
(2) Shen, Z.; Burrows, P. E.; Bulović, V.; Forrest, S. R.; Thompson, M. E. *Science* **1997**, *276*, 2009–2011.
(3) Ng, H. T.; Fang, A.; Huang, L.; Li, S. F. Y. *Langmuir* **2002**, *18*, 6324–6329.
(4) Garcia, G.; Buonsanti, R.; Runnerstrom, E. L.; Mendelsberg, R. J.; Llordes, A.; Anders, A.; Richardson, T. J.; Milliron, D. J. *Nano Lett.* **2011**, *11*, 3315–4420.
(5) Tahar, R. B. H.; Ban, T.; Ohya, Y.; Takahashi, Y. *J. Appl. Phys.* **1998**, *83*, 2631–2645.
(6) Han, H.; Adams, D.; Mayer, J. W.; Alford, T. L. *J. Appl. Phys.* **2005**, *98*, 083705–(1–8).
(7) Liu, Q.; Lu, W.; Ma, A.; Tang, J.; Lin, J.; Fang, J. *J. Am. Chem. Soc.* **2005**, *127*, 5276–5277.
(8) Richard, A. G. Jr.; Summers, C. J. *Thin Solid Films* **2009**, *518*, 1136–1139.
(9) Puetz, J.; Aegerter, M. A. *Thin Solid Films* **2008**, *516*, 4495–4501.
(10) Heusing, S.; de Oliveira, P. W.; Kraker, E.; Haase, A.; Palfinger, C.; Veith, M. *Thin Solid Films* **2009**, *518*, 1164–1169.
(11) Kim, K. Y.; Park, S. B. *Mater. Chem. Phys.* **2004**, *86*, 210–221.
(12) Yang, J.; Li, C.; Quan, Z.; Kong, D.; Zhang, X.; Yang, P.; Lin, J. *Cryst. Growth & Des.* **2008**, *8*, 695–699.
(13) Choi, S.-I.; Nam, K. M.; Park, B. K.; Seo, W. S.; Park, J. T. *Chem. Mater.* **2008**, *20*, 2609–2611.
(14) Li, X.; Kale, G. M. *J. Phys.: Conf. Ser.* **2006**, *26*, 319–322.
(15) Giltsrap, R. A.; Capozzi, C. J.; Carson, C. G.; Gerhardt, R. A.; Summers, C. J. *Adv. Mater.* **2008**, *20*, 4163–4166.
(16) Bühler, G.; Thölmann, D.; Feldmann, C. *Adv. Mater.* **2007**, *19*, 2224–2227.
(17) Hakuta, Y.; Seino, K.; Ura, H.; Adschiri, T.; Takizawa, H.; Arai, K. *J. Mater. Chem.* **1999**, *9*, 2671–2674.
(18) Hayashi, H.; Hakuta, Y.; Kurata, Y. *J. Mater. Chem.* **2004**, *14*, 2046–2051.
(19) Lu, J.; Hakuta, Y.; Hayashi, H.; Ohashi, T.; Nagase, T.; Hoshi, Y.; Sato, K.; Nishioka, M.; Inoue, T.; Hamakawa, S. *J. Supercrit. Fluids* **2008**, *46*, 77–82.
(20) Fang, Z.; Assaaoudi, H.; Guthrie, R. I. L.; Kozinski, J. A.; Butler, I. S. *J. Am. Ceram. Soc.* **2007**, *90*, 2367–2371.
(21) Zhang, J.; Ohara, S.; Umetsu, M.; Naka, T.; Hatakeyama, Y.; Adschiri, T. *Adv. Mater.* **2007**, *19*, 203–206.
(22) Adschiri, T. *Chem. Lett.* **2007**, *36*, 1188–1193.
(23) Taguchi, M.; Takami, S.; Naka, T.; Adschiri, T. *Cryst. Growth Des.* **2009**, *9*, 5297–5303.
(24) Yu, J.; Savage, P. E. *Ind. Eng. Chem. Res.* **1998**, *37*, 2–10.
(25) Shimada, S.; Mackenzie, K. J. D. *J. Cryst. Growth* **1981**, *55*, 453–456.
(26) Watanabe, M.; Sato, T.; Inomata, H.; Smith, R. L. Jr.; Arai, K.; Kruse, A.; Dinjus, E. *Chem. Rev.* **2004**, *104*, 5803–5821.
(27) Abdulagatov, I. M.; Bazaev, A. R.; Magee, J. W.; Kiselev, S. B.; Ely, J. F. *Ind. Eng. Chem. Res.* **2005**, *44*, 1967–1984.

J Nanopart Res
DOI 10.1007/s11051-011-0324-0

RESEARCH PAPER

One-pot hydrothermal synthesis of an assembly of magnetite nanoneedles on a scaffold of cyclic-diphenylalanine nanorods

Takanari Togashi · Mitsuo Umetsu · Takashi Naka · Satoshi Ohara · Yoshiharu Hatakeyama · Tadafumi Adschiri

Received: 17 November 2010 / Accepted: 7 March 2011

Abstract The assembly of metal oxide nanoparticles (NPs) on a biomolecular template by a one-pot hydrothermal synthesis method is achieved for the first time. Magnetite (Fe_3O_4) nanoneedles (length: ~100 nm; width: ~10 nm) were assembled on cyclic-diphenylalanine (cFF) nanorods (length: 2–10 μm; width: 200 nm). The Fe_3O_4 nanoneedles and cFF nanorods were simultaneously synthesized from $FeSO_4$ and L-phenylalanine by hydrothermal synthesis (220 °C and 22 MPa), respectively. The samples were analyzed by powder X-ray diffraction (XRD), Fourier transform infrared spectroscopy (IR), transmission electron microscopy (TEM), and superconducting quantum interference device (SQUID) magnetometry. Experimental results indicate that Fe_3O_4 nanoneedles were assembled on cFF nanorods during the hydrothermal reaction. The composite contained 3.3 wt% Fe_3O_4 nanoneedles without any loss of the original magnetic properties of Fe_3O_4.

Keywords Self-assembly · Magnetite · Peptide · Hydrothermal · One-pot synthesis

Electronic supplementary material The online version of this article (doi:10.1007/s11051-011-0324-0) contains supplementary material, which is available to authorized users.

T. Togashi (✉) · T. Adschiri
Advanced Institute for Material Research,
Tohoku University, 2-1-1, Katahira, Aoba-ku,
Sendai 980-8577, Japan
e-mail: togashi@tagen.tohoku.ac.jp

M. Umetsu
Department of Biomolecular Engineering, Graduate School of Engineering, Tohoku University, Aoba 6-6-11-608 Aramaki, Aoba-ku, Sendai 980-8579, Japan

T. Naka
Innovative Materials Engineering Laboratory,
National Institute for Material Science, Sengen 1-2-1,
Tsukuba, Ibaraki 305-0047, Japan

S. Ohara
Joining and Welding Research Institute,
Osaka University, 11-1 Mihogaoka, Ibaraki,
Osaka 567-0047, Japan

Y. Hatakeyama
Institute for Multidisciplinary for Advanced Material,
Tohoku University, 2-1-1 Katahira, Aoba-ku, Sendai,
Miyagi 980-8577, Japan

Introduction

At present, it is considered that the hierarchical structures formed by the self assembly of nanoparticles (NPs) of inorganic materials such as metals, semiconductors, and ceramics can be used to develop novel electronic, magnetic, and optical devices on account of certain interactions between the excitons, magnetic moments, or surface plasmons of individual NPs (Nie et al. 2010). Many research groups have reported the assembly of isotropic 2D and 3D NPs using various techniques to form structures such as

Published online: 23 March 2011

films/sheets and superlattice crystals (Pileni 2001; Collier et al. 1998; Claridge et al. 2009; Gasser 2009). In contrast, few studies have demonstrated the assembly of anisotropic structures such as rods or fibers, probably on account of the difficulties involved in the preparation of such structures along anisotropic directions (Tang and Kotov 2005).

Biomaterials are highly ordered from the molecular scale to the nano- and microscales, often in a hierarchical manner; most functional hard tissues are characterized by intricate nanostructure comprising biomolecules and inorganic materials (Sarikaya et al. 2003). It is anticipated that biomolecules can serve as highly powerful tools in the development of scaffolds for NP assembly. In general, inorganic NPs tend to aggregate because of their high surface energy. Consequently, prior to assembly, a solution containing completely dispersed NPs must be prepared. However, the requirement for completely dispersed NPs can be bypassed by the formation of NPs on or in a biomolecular scaffold substrate.

To prepare anisotropic NP assemblies, self-assembling biomolecules such as DNA (Braun et al. 1998; Alivisatos 2004; Hatakeyama et al. 2004), peptides (Banerjee et al. 2005; Sone and Stupp 2004; Fu et al. 2003; Carny et al. 2006), proteins (Scheibel et al. 2003; Patolsky et al. 2004; Platt et al. 2005; Ostrov and Gazit 2010), and polysaccharides (Feng et al. 2005; Wang et al. 2009; Huang and Kunitake 2003) have been used; these biomolecules are utilized not only in applications involving cell manipulation (Hultgren et al. 2003) and drug delivery (Tan et al. 2006) but also as templates for the arrangement of inorganic NPs. In general, approaches involving biomolecular assembly are carried out in aqueous solutions under physiologically mild conditions, because biomolecules are typically hydrophobic and heat-labile. However, a high temperature is usually required to obtain high-quality inorganic material.

In our previous study, we synthesized cyclic-diphenylalanine (cFF) crystals from L-phenylalanine (L-Phe) with a high yield by hydrothermal treatment, and we found that excess cFF synthesis caused the spontaneous assembly of cFF crystals with a rod-like morphology (Togashi et al. 2006). Interestingly, the reaction conditions used for the synthesis of cFF nanorods can also be utilized to synthesize organic modified metal oxide NPs (Byrappa and Adschiri 2007; Yoshimura and Byrappa 2008). We consider that cFF nanorods and metal oxide NPs can be simultaneously synthesized and that cFF nanorods can be utilized as a template for metal oxide NP assembly.

In this report, we propose a one-pot synthesis method to assemble metal oxide NPs on a biomolecular template in water at high temperature and pressure. L-Phe and iron ions were used for synthesizing cFF and magnetite (Fe_3O_4) NPs, respectively. In addition, the synthesized Fe_3O_4 was conjugated on cFF rods during the reaction.

Experimental

Chemicals

L-Phenylalanine (L-Phe) and iron sulfide ($FeSO_4$) and potasium hydroxide (KOH) were purchased from Wako Pure Chemical Industries Ltd. and used without further purification.

Synthesis

A pressure-resistant tube reactor (SUS 316) with an inner volume of 5.0 mL was used for the hydrothermal synthesis of cFF and the cFF–Fe_3O_4 conjugate. For synthesizing the cFF–Fe_3O_4 conjugate, 0.49 g of L-Phe powder was placed in the reactor, after which 2.14 mL of 100 mM $FeSO_4$ aqueous solution and 2.14 mL of 200 mM KOH aqueous solution were added and the reactor was heated in an electric furnace controlled at 220 °C to carry out the reaction. The estimated pressure inside the reactor at 220 °C is 22 MPa. After 30 min, the reaction was terminated by cooling the reactor in a water bath at room temperature. The products were washed by three cycles of centrifugation at 9200*g* for 30 min, decantation, and redispersion into double distilled water (ddH_2O) to remove unreacted L-Phe and water-soluble chemicals. The obtained products were dried under vacuum at room temperature. For synthesizing cFF and Fe_3O_4 NPs, the $FeSO_4$ and KOH solution was replaced with water and the concentration of L-Phe was varied in the range 0–100 mM, respectively.

Analysis

Transmission electron microscopy (TEM) and high-resolution TEM (HRTEM) were performed on a JEM-1200 EXII electron microscope (JEOL Ltd., Japan) operating at 120 kV and a Hitachi H-7100 electron microscope (Hitachi Inc, Japan) operating at 200 kV, respectively. The samples were dispersed in ddH_2O and the dispersed samples were dropped on a carbon-coated copper grid. For the products, attenuated total reflectance Fourier transform infrared (ATR FT-IR) spectra were measured on a FT/IR680 spectrometer (Jasco Corp., Japan). Powder X-ray diffraction (XRD) patterns of the products were recorded on a Rigaku RINT 2000 system (Rigaku, Japan) using Cu Kα radiation at 2θ values ranging from 10° to 80°. The oriented particulate monolayer XRD (OPML-XRD) method was also employed to analyze the sample. To prepare the sample for OPML-XRD, a few drops of 3 wt% gelatine solution containing 1 wt% sample powder was evenly spread over a glass plate and dried overnight at room temperature; by using this procedure, the direction of alignment of the elongated crystals could be controlled such that it was parallel to the plane of the glass plate.

Result and discussion

In order to analyze the crystal growth direction of the cFF nanorods in the precipitates synthesized by the hydrothermal reaction of L-Phe without $FeSO_4$, the products were analyzed using powder X-ray diffraction (XRD) and the OPML-XRD method (Fig. 1). The powder XRD pattern of the products (Fig. 1b) was similar to the diffraction pattern of single cFF crystals calculated using the single crystal geometry data for cFF reported by Gdaniec et al. (Fig. 1a) (Gdaniec and Liberek 1986). The OPML-XRD pattern (Fig. 1c) revealed three peaks that were assigned to the diffractions of the (012), (024), and (018) facets of the cFF crystal. The OPML-XRD method was used to estimate the Miller indices of the facets of the polyhedral microcrystals, the basal plane of the pellet particle, and the evolution axis of elongated particles (Sugimoto et al. 1993). The estimation results revealed that anisotropic crystals were laid on the glass plate surface, with their axes

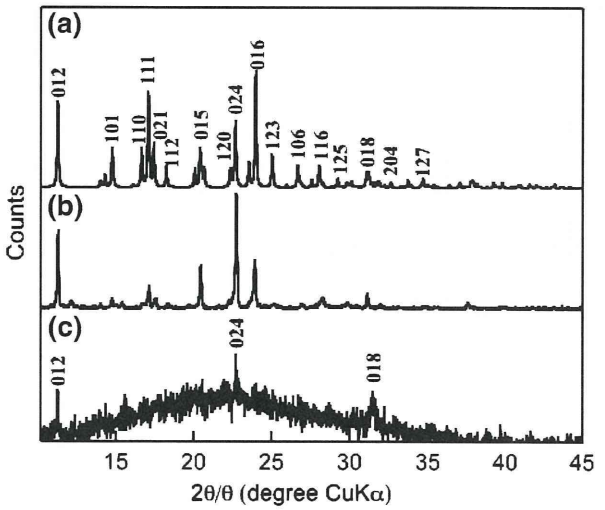

Fig. 1 XRD pattern of cFF. (*a*) Diffraction pattern calculated using single crystal geometry data, (*b*) XRD pattern of cFF synthesized by hydrothermal reaction at 220 °C and 22 MPa for 30 min, and (*c*) OPML-XRD pattern of synthesized cFF

positioned parallel to the plane of the glass plate, thereby indicating that the cFF nanorods grew along the *x*-axis. Figure 2 shows the single crystal geometry of cFF. Intermolecular hydrogen bonds of diketopiperadine are formed through amide group linkages along the *x*-axis. These intermolecular hydrogen bonds of the amide groups may serve as a driving force in the formation of anisotropic cFF nanorods (Fig. 2).

Figure 3 shows photographs of the products that were obtained by the hydrothermal treatment of L-Phe and $FeSO_4$ solutions at 220 °C and 22 MPa for 30 min. As previously reported, the hydrothermal treatment of 100 mM L-Phe solution led to the synthesis of a small amount of cFF (Togashi et al. 2006), but an increase in the L-Phe concentration to 710 mM led to the synthesis of a large amount of cFF (Fig. 3a(i)). The hydrothermal reaction of 100 mM L-Phe in a 50 mM $FeSO_4$ solution resulted in the formation of a black-colored insoluble product (Fig. 3a(ii)); however, an increase in the L-Phe concentration to 710 mM led to the formation of a brown-colored aggregate (Fig. 3a(iii)). The black- and brown-colored products synthesized in the 50 mM $FeSO_4$ solution were attracted toward a permanent magnet generating a magnetic field of 0.35 T at the magnet surface (Fig. 3b), while the aggregates synthesized without $FeSO_4$ were not attracted by the applied external magnetic field

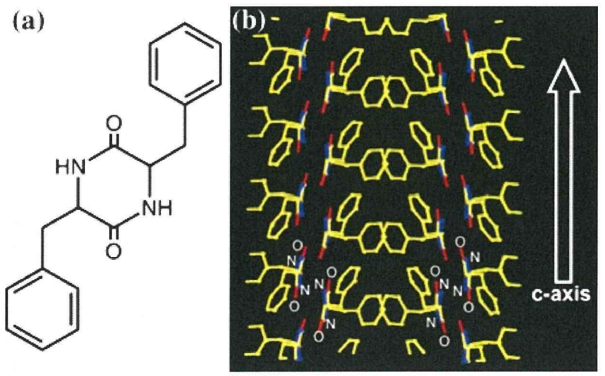

Fig. 2 (*a*) Chemical structure of L-Phe (*b*) Rod-like assembly model of the single crystal structure (This figure appear in color in online, *yellow*: carbon atom, *blue*: nitrogen atom, *red*: oxygen atom)

(Fig. 3(i)). These results imply the formation of a magnetic iron oxide such as magnetite (Fe_3O_4) or maghemite (γ-Fe_2O_3) during the hydrothermal reaction.

The powder XRD patterns of the products (Fig. 4) were measured in order to identify magnetic materials in the black- and brown-colored products synthesized from L-Phe with $FeSO_4$ (Fig. 4). The black-colored products synthesized from 100 mM L-Phe in 50 mM $FeSO_4$ could satisfactorily be assigned to spinel-type iron oxide, Fe_3O_4, or γ-Fe_2O_3 (Fig. 4a). Further, the crystalline phase was identified as Fe_3O_4 from the lattice parameter calculated using the d-value of the {311} plane; this parameter was evaluated to be 8.40 Å on the basis of the reported lattice parameters of γ-Fe_2O_3 (8.346 Å; JCPDS: 39-1346) and Fe_3O_4 (8.396 Å; JCPDS: 79-4190). Thus, the synthesized magnetic materials were identified as Fe_3O_4. The powder XRD pattern of the brown-colored products revealed small diffraction peaks that were assigned to the (220), (311), and (440) planes of spinel-type iron oxide (closed circles in Fig. 4c), whereas it also revealed some intense peaks in the lower angle region (10–30°) that were well matched with those of cFF (Fig. 4b, c).

To obtain additional data for characterization of spinel-type iron oxide, the brown-colored product was measured by FT-IR spectrum. Before measurement, the brown-colored product was washed with dimethyl sulfoxide (DMSO) and methanol to remove cFF that included in brown-colored product, and the color of the obtained sample was black (see Fig. S1 in Supporting Information). Figure 5 shows the FT-IR spectra of purchased Fe_3O_4, γ-Fe_2O_3, these are used as references, and samples that were obtained from brown-colored products by washing with DMSO. The IR-spectrum of purchased Fe_3O_4, one broad peak at 578 cm^{-1} can be seen and this band is assigned as Fe–O bond of Fe_3O_4 (Fig. 5a) (Cornell and Schwertmann 2003). In the IR spectrum of γ-Fe_2O_3, the broad bands at 698, 638, 580, and 562 cm^{-1} can be seen (Fig. 5b) these are assigned as Fe–O bond of γ-Fe_2O_3 (Cornell and Schwertmann 2003). The IR spectrum of sample has broad band at 576 cm^{-1} and no additional peaks (Fig. 5c). This result strongly support to assignment of the contained iron oxide as Fe_3O_4. Therefore, we conclude that the brown-colored products were composed of Fe_3O_4 and cFF.

To observe the morphology of the synthesized Fe_3O_4 particle and cFF–Fe_3O_4 conjugate, transmission electron microscopy (TEM) images were obtained (Figs. 6, 7). Figure 6a shows the TEM

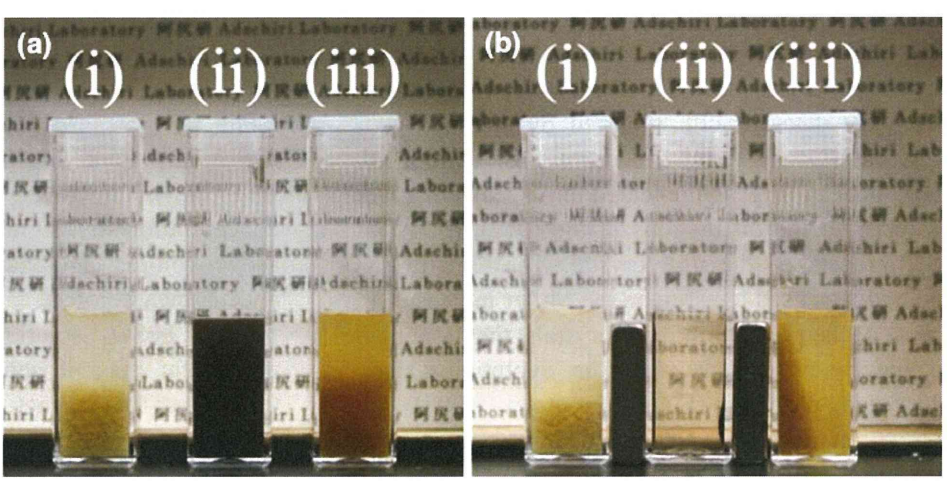

Fig. 3 Photographs of the synthesized products in a plastic cuvette. The products were synthesized by hydrothermal treatment of (*i*) 710 mM L-Phe, (*ii*) 100 mM L-Phe and 50 mM $FeSO_4$, and (*iii*) 710 mM L-Phe and 50 mM of $FeSO_4$ at 220 °C and 22 MPa for 30 min. *Left*: Without external magnetic field. *Right*: With external magnetic field for 5 min

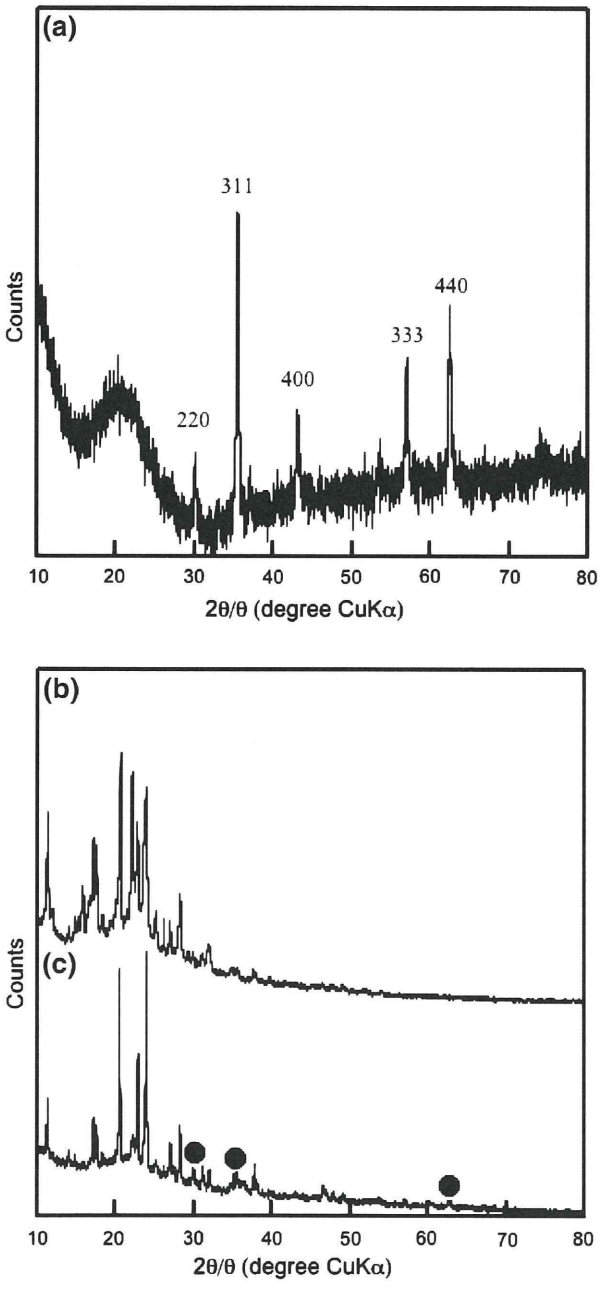

Fig. 4 XRD patterns of the crystals synthesized using (*a*) 100 mM L-Phe and 50 mM $FeSO_4$, (*b*) 710 mM L-Phe, and (*c*) 710 mM L-Phe and 50 mM $FeSO_4$

image of Fe_3O_4 synthesized from 100 mM L-Phe in 50 mM $FeSO_4$. The image reveals needle-like structures with widths and lengths of ~10 and ~100 nm, respectively. The distance between two adjacent points perpendicular to the long axis of a Fe_3O_4 nanoneedle is ~3 Å (Fig. 6b), which corresponds to the lattice spacing of the (220) plane of Fe_3O_4.

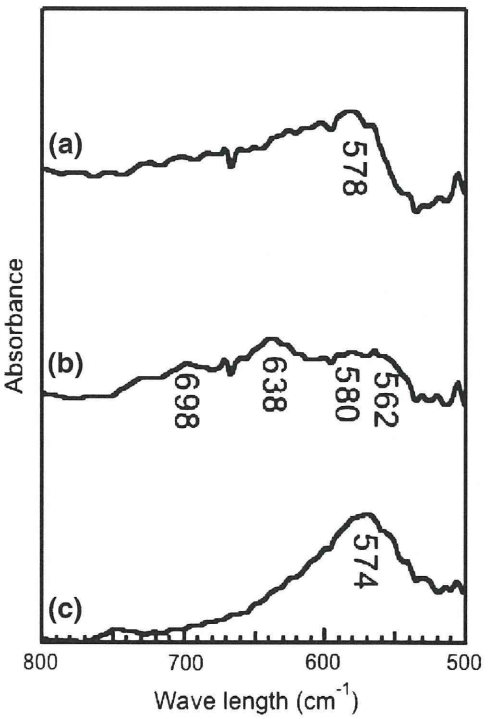

Fig. 5 FT-IR spectrum of (*a*) purchased Fe_3O_4, (*b*) purchased γ-Fe_2O_3, and (*c*) sample

Fe_3O_4 particles synthesized by hydrothermal treatment without L-Phe have spherical or cubic shapes with particle sizes ranging from 50 nm to 100 nm (see Fig. S2a in Supporting Information). As the concentration of L-Phe is increased, the particle shape changes from a spherical shape to a needle-like shape (see Fig. S2b and c in Supporting Information). The order of surface energy of the different facets is $\{111\} < \{100\} < \{110\}$ for the fcc structure (Fan et al. 2009); therefore, the organic molecules predominantly bind to the facet that has a higher surface energy (Xia et al. 2009). Our results suggest that the capping of L-Phe on the (110) surface suppressed the growth of the (220) plane.

Figure 7 shows the TEM images of the synthesized cFF–Fe_3O_4 conjugate. The materials have large rod-like morphologies with widths of 200 nm and lengths of 2–10 μm (Fig. 7a), into which needle-shaped Fe_3O_4 particles are stacked (Fig. 7b). Previously, we reported that the hydrothermal treatment of 710 mM L-Phe in ddH_2O resulted in the formation of a cFF aggregate with a rod-like morphology such that the particles had diameters of 200–500 nm and lengths of 5–10 μm (Togashi et al. 2006). The

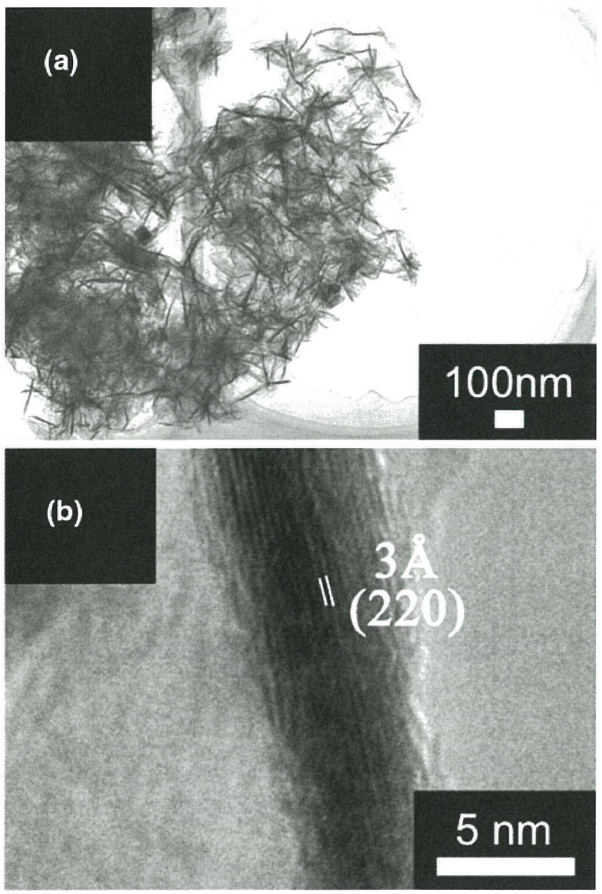

Fig. 6 TEM images of the synthesized Fe_3O_4. **a** TEM image and **b** HRTEM image

TEM images in this study implied that the self-assembly of cFF to form a rod-like morphology was not affected by the simultaneous synthesis of needle-shaped Fe_3O_4 NPs.

To evaluate magnetic property of the products and the mass of Fe_3O_4 in the cFF–Fe_3O_4 conjugate, superconducting quantum interference device (SQUID) magnetometry of the cFF–Fe_3O_4 conjugate was performed. The magnetic properties of the cFF–Fe_3O_4 conjugate and the synthesized needle-shaped Fe_3O_4 NPs were measured by using SQUID at 300 K (Fig. 8). The saturation moments of the cFF–Fe_3O_4 conjugate and the needle-shaped Fe_3O_4 NPs were 2.18 and 63.45 emu/g, respectively (Fig. 8a). However, the needle-shaped Fe_3O_4 NPs included the 4.3 wt% of organic molecules (see Fig. S3a in Supporting Information). To estimate the contribution of the Fe_3O_4 particles in the Fe_3O_4 nanoneedle, $M_{Fe_3O_4}$, was calculated using the equation described below

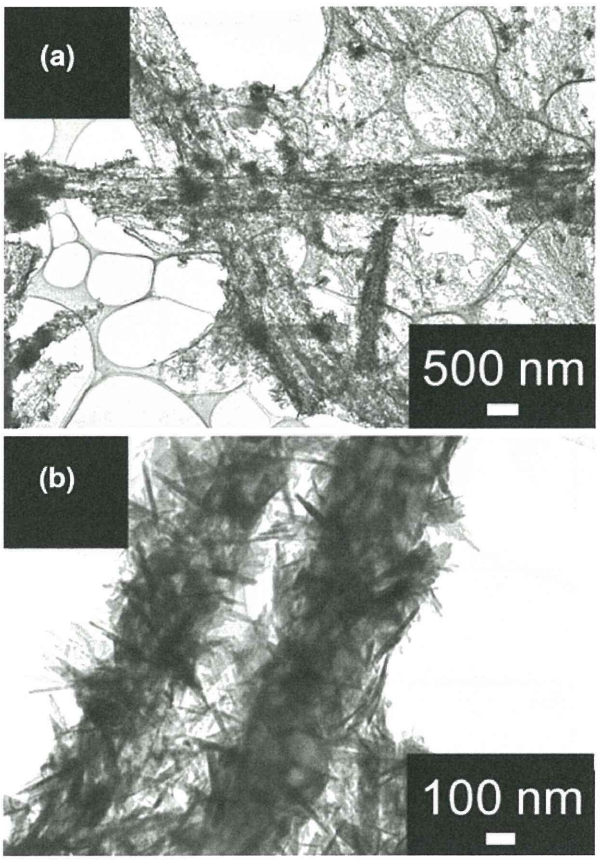

Fig. 7 TEM images of the synthesized cFF–Fe_3O_4 conjugate. **a** Low magnification and **b** high magnification

$$M_{Fe_3O_4} = \frac{M_{observed}}{(W_{sample} - W_{org})}$$

where $M_{observed}$, W_{sample}, and W_{org}, are the observed saturation magnetization value of the Fe_3O_4 nanoneedle with SQUID, the weight of the measured Fe_3O_4 nanoneedle, and the weight of the organic molecules included in the needle-shaped Fe_3O_4 NPs as estimated by TG measurement data respectively. The saturation magnetic moment of pure Fe_3O_4 included in the Fe_3O_4 nanoneedle was 66.58 emu/g. The amount of Fe_3O_4 present in the cFF–Fe_3O_4, $W_{Fe_3O_4}$, was calculated using the equation described below

$$W_{Fe_3O_4} = \frac{M_{cFF-Fe_3O_4}}{M_{Fe_3O_4}}$$

where $W_{Fe_3O_4}$, $M_{cFF-Fe_3O_4}$, and $M_{Fe_3O_4}$, are the amount of Fe_3O_4 present in the cFF–Fe_3O_4, the observed magnetization value of Fe_3O_4, and the calculated magnetization value of the needle-shaped Fe_3O_4 NPs,

respectively. The amount of Fe_3O_4 present in the cFF–Fe_3O_4 was 3.3 wt%.

Both the TEM and SQUID results indicate that the Fe_3O_4 nanoneedle were present on the surface of the cFF nanorods. In addition, the cFF–Fe_3O_4 conjugate and Fe_3O_4 nanoneedle showed almost the same coercivity about 100 Oe at 300 K (Fig. 8b).

To obtain information regarding the organic molecular structure, the Fourier transform infrared (FT-IR) spectra were measured (Fig. 9). In the case of the cFF–Fe_3O_4 conjugate (Fig. 9b), all peaks were identical to those of cFF synthesized without Fe_3O_4 (Fig. 9a). In addition, the FT-IR patterns were well matched with that of cFF synthesized using a previously described organic synthesis method (Brown et al. 1965). This result suggests that cFF constitutes the only organic component in the cFF–Fe_3O_4 conjugate.

The FT-IR spectra of L-Phe and the synthesized needle-shaped Fe_3O_4 NPs are shown in Fig. 9c and d, respectively. All the peaks in the L-Phe spectrum were assigned as per the data provided by Mahalakshmi et al. (2006) (see Table S1 in Supporting Information). In the FT-IR spectrum of the synthesized Fe_3O_4 (Fig. 9d), a broad band at 1584 cm^{-1} is visible; this band can be assigned as $n_{as}(COO^-)$ bound to the transition metal (Nakamoto 1970). Furthermore, the peaks at 1493, 1453, 1410, 1308, 1152, 1018, and 849 cm^{-1} can be assigned as $\beta_s(NH_3^+)$, $\nu(C–C)_{ring}$ + $b_s(CH_2)$, $n_s(COO^-)$, $\gamma_{as}(CH_2)$, $\delta(C–H)_{ring}$, $\Delta(C–H)_{ring}$, and $\gamma(C–H)_{ring}$, respectively. Thus, the obtained results

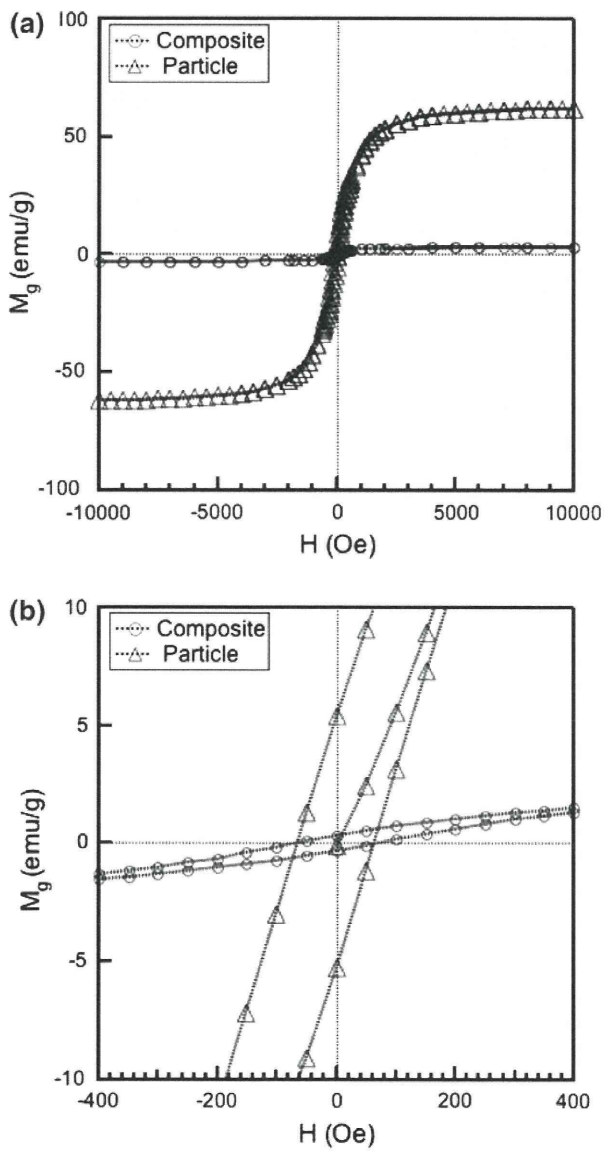

Fig. 8 Magnetic properties of the synthesized materials at 300 K (*open circle*: cFF–Fe_3O_4 conjugate, *open triangle*: synthesized Fe_3O_4 with 100 mM L-Phe)

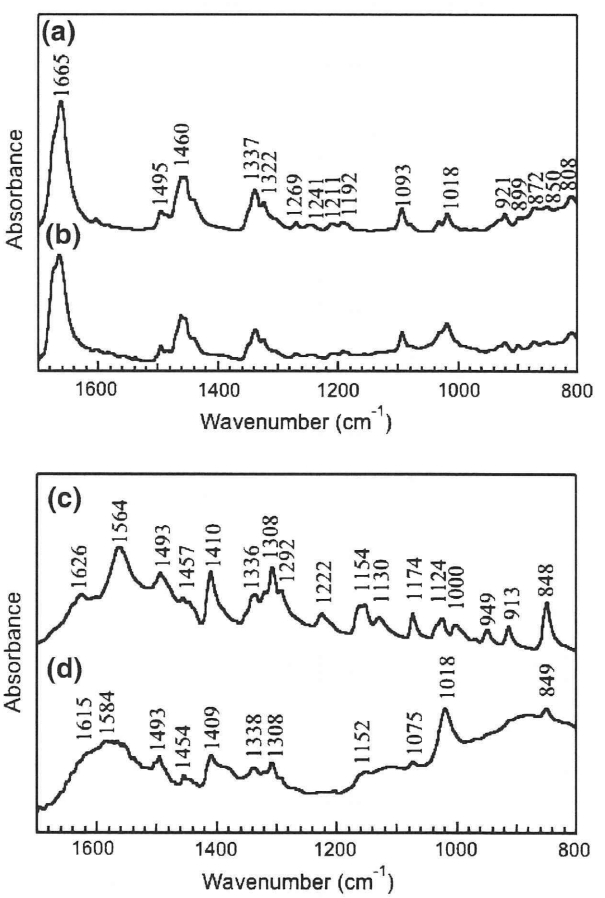

Fig. 9 FT-IR spectrum of (*a*) synthesized crystals with 710 mM of L-Phe, (*b*) synthesized crystal with 710 mM L-Phe and 50 mM $FeSO_4$, (*c*) pure L-Phe, and (*d*) synthesized crystal with 100 mM L-Phe and 50 mm $FeSO_4$

suggest the conjugation of L-Phe on Fe_3O_4 during the hydrothermal reaction.

Carny et al. reported that peptide-coated gold (Au) NPs could bind with peptide-based nanofibers in an aligned manner (Carny et al. 2006). The peptide that was conjugated on the Au NPs exhibited affinity toward the peptide nanofiber; as a result, the conjugated Au NPs could interact with the peptide nanofiber. This peptide–peptide interaction may constitute one of the main driving forces in the arrangement of Au NPs on the peptide nanofiber. In our study, the synthesized Fe_3O_4 nanoneedle is covered with L-Phe. The conjugated L-Phe and synthesized cFF have an aromatic ring at their side chain. It is possible that these aromatic rings undergo p–p interactions with each other. Thus, we consider that the π–π interaction between cFF and L-Phe conjugated on the Fe_3O_4 nanoneedle serves as one of the driving forces in the adherence of the Fe_3O_4 nanoneedles to the cFF nanorod.

A cFF–Fe_3O_4 conjugate was synthesized in situ by a one-pot hydrothermal reaction. The morphology of Fe_3O_4 changed from spherical and cubic shapes to a needle-like shape on account of the capping of L-Phe on the Fe_3O_4 surface. Fe_3O_4 nanoneedles were assembled on cFF rod-like crystals by hydrothermal synthesis under a high cFF concentration. This method may be applied to the production of NP arrays of various metal oxides from metal ions and amino acids and to the synthesis of rod-like cFF–metal oxide NP hybrids.

Conclusion

A cFF–Fe_3O_4 conjugate was synthesized in situ by a one-pot hydrothermal reaction. The morphology of Fe_3O_4 changed from spherical and cubic shapes to a needle-like shape on account of the capping of L-Phe on the Fe_3O_4 surface. Fe_3O_4 nanoneedles were assembled on cFF rod-like crystals by hydrothermal synthesis under a high cFF concentration. This method may be applied to the production of NP arrays of various metal oxides from metal ions and amino acids, L-Phe, and to the synthesis of rod-like cFF–metal oxide NP hybrids.

Acknowledgment This work was partly supported in part by a Grant-in-Aid for the COE project Giant Molecules and Complex Systems, 2002.

References

Alivisatos P (2004) The use of nanocrystals in biological detection. Nat Biotechnol 22:47–52. doi:10.1038/nbt927

Banerjee IA, Yu L, Matsui H (2005) Room-temperature Wurtzite ZnS nanocrystal growth on Zn finger-like peptide nanotubes by controlling their unfolding peptide structures. J Am Chem Soc 127:16002–16003. doi:10.1021/ja054907e

Braun E, Eichen Y, Sivan U, Ben-Yoseph G (1998) DNA-templated assembly and electrode attachment of a conducting silver wire. Nature 391:775–778. doi:10.1038/35826

Brown R, Kelley C, Wiberley SE (1965) The production of 3-benzylidene-6-isobutylidene-2,5-dioxopiperazine, 3,6-dibenzylidene-2,5-dioxopiperazine, 3-benzyl-6-benzylidene-2,5-dioxopiperazine, and 3,6-dibenzyl-2,5-dioxopiperazine by a variant of *Streptomyces noursei*. J Org Chem 30:277–280. doi:10.1021/jo01012a066

Byrappa K, Adschiri T (2007) Hydrothermal technology for nanotechnology. Prog Cryst Growth Chem 53:117–166. doi:10.1016/j.pcrysgrow.2007.04.001

Carny O, Shelev DE, Gazit E (2006) Fabrication of coaxial metal nanocables using a self-assembled peptide nanotube scaffold. Nano Lett 6:1594–1597. doi:10.1021/nl0604681

Claridge SA, Castleman AW, Khanna SN, Murray CB, Sen A, Weiss PS (2009) Cluster-assembled materials. ACS Nano 3:244–255. doi:10.1021/nn800820e

Collier CP, Vossmeyer T, Hearth JR (1998) Nanocrystal superlattices. Annu Rev Phys Chem 49:371–404. doi:10.1146/annurev.physchem.49.1.371

Cornell RM, Schwertmann U (2003) The iron oxides, 2nd edn. Wiley–VCH Verlag GmbH & Co

Fan HM, Yi JB, Yang Y, Kho KW, Tan HR, Shen ZX, Ding J, Sun XW, Olivo MC, Feng YP (2009) Single-crystalline MFe_2O_4 nanotubes/nanorings synthesized by thermal transformation process for biological applications. ACS Nano 3:2798–2808. doi:10.1021/nn9006797

Feng J, Miedaner A, Ahrenkiel P, Himmel ME, Curtis C, Ginley D (2005) Self-assembly of photoactive TiO_2-cyclodextrin wires. J Am Chem Soc 127:14968–14969. doi:10.1021/ja054448h

Fu X, Wang Y, Huang L, Sha Y, Gui L, Lai L, Tang Y (2003) Assemblies of metal nanoparticles and self-assembled peptide fibrils—formation of double helical and single-chain arrays of metal nanoparticles. Adv Mater 15:902–906. doi:10.1002/adma.200304624

Gasser U (2009) Crystallization in three- and two-dimensional colloidal suspensions. J Phys Condens Mater 21:203101-1-14. doi:10.1088/0953-8984/21/20/200301

Gdaniec M, Liberek B (1986) Structure of cyclo(-L-phenylalanyl-L-phenylalanyl-). Acta Crystallogr Sect C: Cryst Struct Commun 42:1343–1345. doi:10.1107/S0108270186092338

Hatakeyama Y, Minami M, Ohara S, Umetsu M, Takami S, Adschiri T (2004) Control of designed high-order DNA conformation as a template for nano particle assembly. Kobunshironbunsyu 61:617–622

Huang J, Kunitake T (2003) Nano-precision replication of natural cellulosic substances by metal oxides. J Am Chem Soc 125:11834–11835. doi:10.1021/ja037419k

Hultgren A, Tanase M, Chen CS, Meyer GJ, Reiche DH (2003) Cell manipulation using magnetic nanowires. J Appl Phys 93:7554–7556. doi:10.1063/1.1556204

Mahalakshmi R, Jesuraja SX, Jerome DS (2006) Growth and characterization of L-phenylalanine. Cryst Res Technol 41:780–783. doi:10.1002/crat.200510668

Nakamoto K (1970) Infrared spectra of inorganic and coordination compounds, 2nd edn. Willy–Interscience, pp 232–239

Nie Z, Petukhova A, Kumacheva E (2010) Properties and emerging applications of self-assembled structures made from inorganic nanoparticles. Nat Nanotechnol 5:15–25. doi:10.1038/nnano.2009.453

Ostrov N, Gazit E (2010) Genetic engineering of biomolecular scaffolds for the fabrication of organic and metallic nanowire. Angew Chem Int Ed 49:3018–3021. doi:10.1002/anie.200906831

Patolsky F, Weizmann Y, Willner I (2004) Actin-based metallic nanowires as bio-nanotransporters. Nat Mater 3:692–695. doi:10.1038/nmat1205

Pileni MP (2001) Nanocrystal self-assemblies: fabrication and collective properties. J Phys Chem B 105:3358–3371. doi:10.1021/jp0039520

Platt M, Muthukrishnan G, Hancock WO, Williams ME (2005) Millimeter scale alignment of magnetic nanoparticle functionalized microtubles in magnetic fields. J Am Chem Soc 127:15686–15687. doi:10.1021/ja055815s

Sarikaya M, Tamerler C, Jen AK-Y, Schulten K, Baneyx F (2003) Molecular biomimetics: nanotechnology through biology. Nat Mater 2:577–585. doi:10.1038/nmat964

Scheibel T, Parthasarathy R, Sawicki G, Lin XM, Jaeger H, Lindquist SL (2003) Conducting nanowires built by controlled self-assembly of amyloid fibers and selective metal deposition. Proc Natl Acad Sci USA 100:4527–4532. doi:10.1073_pnas.0431081100

Sone ED, Stupp SI (2004) Semiconductor-encapsulated peptide-amphiphile nanofibers. J Am Chem Soc 126:12756–12757. doi:10.1021/ja0499344

Sugimoto T, Muramatsu A, Sakata K, Shindo D (1993) Characterization of hematite particles of different shapes. J Colloid Interf Sci 158:420–428. doi:10.1006/jcis.1993.1274

Tan ST, Wendorff JH, Pietzonka C, Jia ZH, Wang GQ (2006) Biocompatible and biodegradable polymer nanofibers displaying superparamagnetic properties. Chem Phys Chem 6:1461–1465. doi:10.1002/cphc.200500167

Tang T, Kotov NA (2005) One-dimensional assemblies of nanoparticles: preparation, properties, and promise. Adv Mater 17:951–962. doi:10.1002/adma.200401593

Togashi T, Umetsu M, Tsuchizaki H, Ohara S, Naka T, Adschiri T (2006) Simultaneous synthesis and self-assembly of cyclic diphenylalanine at hydrothermal condition. Chem Lett 35:636–637. doi:10.1246/cl2006.636

Wang Y, Li YF, Huang CZ (2009) A one-pot green method for one-dimensional assembly of gold nanoparticles with a novel chitosan-ninhydrin bioconjugate at physiological temperature. J Phys Chem C 113:4315–4320. doi:10.1021/jp809708q

Xia Y, Xiong Y, Lim B, Skrabalak SE (2009) Shape-controlled synthesis of metal nanocrystals: simple chemistry meets complex physics? Angew Chem Int Ed 48:60–103. doi:10.1002/anie.200802248

Yoshimura M, Byrappa K (2008) Hydrothermal processing of materials: past, present and future. J Mater Sci 43:2085–2103. doi:10.1007/s10853-007-1853-x

Langmuir

LETTER

pubs.acs.org/Langmuir

Biomimetic Engineering of Modular Bispecific Antibodies for Biomolecule Immobilization

Hideki Watanabe,[†,‡] Kengo Kanazaki,[†] Takeshi Nakanishi,[†] Hidenori Shiotsuka,[§] Satoru Hatakeyama,[§] Masaru Kaieda,[§] Takeshi Imamura,[§] Mitsuo Umetsu,[†] and Izumi Kumagai*[,†]

[†]Department of Biomolecular Engineering, Graduate School of Engineering, Tohoku University, Aoba 6-6-11, Aramaki-aza, Aoba-ku, Sendai 980-8579, Japan

[‡]National Institute of Advanced Industrial Science and Technology (AIST), Central 6, Tsukuba 305-8566, Japan

[§]Nanobiotechnology Research Division, Canon Research Center, Canon Inc., Shimomaruko 3-30-2, Ohta-ku, Tokyo 146-8501, Japan

Supporting Information

ABSTRACT: Modular bispecific antibodies (BsAb's) that interact directly with a gold surface were engineered for immobilization on biosensing devices. The BsAb's consist of the variable fragments of antigold and antilysozyme antibodies connected via one of three linkers derived from naturally occurring proteins. The BsAb's were bound tightly to both the gold surface and to lysozyme, thus functioning as interface molecules between lysozyme and the gold surface without a substantial loss of antigen-binding activity. The antigen-binding capacity (the ratio of the amount of immobilized lysozyme to the amount of immobilized BsAb) on the gold surface reached 82%. An analysis of the correlation between binding capacity and linker characteristics indicated that the presence of a long, rigid linker sequence derived from a cellulase resulted in a higher antigen-binding capacity than did the presence of a long but relatively flexible glycine-rich linker. This result suggests a strategy for designing linkers suitable for BsAb-based biomolecular immobilization.

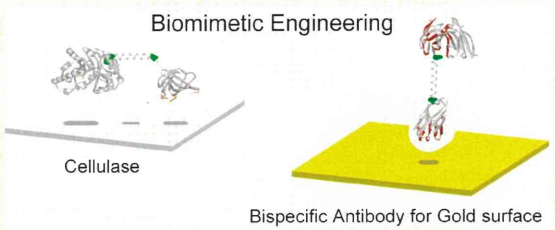

INTRODUCTION

Biomolecular recognition has made possible the use of bioprobes to detect small quantities of target molecules in crude samples.[1] Antibodies are attractive bioprobes because they have a high affinity and specificity for their target antigens, and antibodies have been widely used for immunoassays and the biosensing of various antigens,[2] toxins,[3] and cancer markers.[4] In antibody-based biosensing systems, immobilization of the antibodies on solid-phase supports is indispensable for capturing target antigens and transducing the target information into a detectable signal. Physical adsorption and covalent cross-linking such as thiol chemistry or *N*-hydroxysuccinimide/*N*-ethyl-*N*′-dimethylaminopropylcarbodiimide (NHS/EDC) chemistry are methods commonly used for immobilizing proteins. However, these methods are subject to problems[5,6] such as the structural deformation of the proteins on the solid phase, random orientation of the proteins, low immobilization yields, and the complexity of the procedure. To control the orientation of proteins on solid substrates, proteins have been modified with various affinity tags. For example, proteins with polyhistidine tags fused at the terminus can be orientationally immobilized on solid substrates with nickel-resin surfaces,[7] and antigen peptides such as c-myc,[8] FLAG peptides,[9] and biotinylated peptides[10] can also be used to control protein orientation at surfaces. Staphylococcal protein A, which can specifically recognize the Fc fragment in antibodies, is also utilized to control the orientation of immobilized proteins, and recent technology with enzymatic reactions had enabled the site-selective immobilization of protein A on phospholipid polymer surface to immobilize antibodies in a single direction.[11] These protein immobilization can control the direction of immobilized proteins; however, in many cases, surface fabrication of substrate and complicated conjugation processes should be necessary for protein immobilization.[12]

In this study, we developed a protein immobilization method without the need for surface fabrication of the substrate or complicated conjugation processes, utilizing a novel type of antibody with an affinity for a material surface. Recently, we generated an antigold antibody (A14P-b2) with a high affinity (K_D = 1.7 nM) and specificity for gold surfaces.[13] Here, we utilized the antigold antibody as a binding unit for the immobilization of proteins on biosensing devices with gold surfaces. For the utilization of antigold antibodies for protein immobilization, we designed a modular bispecific antibody (BsAb). We suspected that a modular structure, that is, a structure in which the immobilized region and the sensing domain are separated, would effectively retain the binding activity of proteins immobilized on a solid surface while avoiding deleterious effects on the conformation and function of the sensing domain. Modular structures are

Received: February 17, 2011
Revised: June 16, 2011
Published: July 07, 2011

found in naturally occurring proteins; we therefore believed that a biomimetic approach to the autonomic immobilization of modular antibodies with a native antigen-binding capacity for use as biosensing devices could be fruitful. In this study, we designed three BsAb's with modular structures consisting of three domains: an antigold antibody (for immobilization onto the gold surface), antilysozyme antibody HyHEL10[14] (for immobilizing lysozyme as a model antigen), and one of three linker sequences derived from proteins with modular structures. For the linkers, we focused on three kinds of multisubunit proteins with distinctive linker sequences: a bacterial cellulase,[15,16] which contains a long, rigid linker; filamentous bacteriophage coat protein g3p,[17] which contains a long, flexible linker; and a diabody,[18] which contains a short, flexible linker.

The designed BsAb's were spontaneously bound to the gold surface and retained good antigen-binding activity in their bound states. We also discussed the correlation among the structural characteristics of the different linker regions and their effects on the binding activities. Our results suggest a strategy for designing effective linkers for optimum biosensing performance.

MATERIALS AND METHODS

Linker Design. A rigid, extended linker region was designed on the basis of naturally occurring proteins: bacterial enzymes such as cellulases,[19] chitinases,[20] and polyhydroxybutyrate depolymerase.[21] Cellulases consist of three functionally independent domains:[22,23] a domain that binds to a crystalline cellulose surface, a catalytic domain that hydrolyzes cellulose, and a linker region that connects the other two domains. The linker regions of enzymes such as *Cellulomonas fimi* xylanase Cex[24,25] have distinctive amino acid sequences that are highly enriched in threonine and proline residues, which impart conformational restrictions that lead to rigid structures. We designed a proline- and threonine-rich linker (designated PT21) with a length of 21 amino acid residues, derived from this cellulase.

Flexible linkers also occur in vivo and are used in protein engineering to link two domains so that their functions are not hindered. Filamentous bacteriophage fd coat protein g3p, which is composed of three domains, has a very flexible linker region containing glycine-rich repeat units (referred to as glycine-rich region 2). This protein plays a major role in infection processes.[17] We used this region as a flexible linker with a length of 31 amino acid residues; this glycine-rich linker is designated as GR31.

We also used a conventional antibody-engineering technique to design a BsAb with a short linker based on a diabody. Diabodies[26] have been developed for clinical uses such as cancer therapy. In contrast to the proteins that we have described so far, diabodies have relatively short linkers (typically less than five amino acid residues) and thus effectively cause the dimerization of scFv's[26] Therefore, we used a diabody to construct a conventional BsAb so that we could compare its antigen-binding capacity with the binding capacities of the modular BsAb's on the gold surface.

The designed linker sequences derived from the modular proteins are listed in Table 1.

Construction of BsAb Expression Vectors. Oligo DNAs were purchased from Nihon Gene Research Laboratory (Sendai, Japan). Gene fragments for the single-chain variable fragment (scFv) from antilysozyme antibody HyHEL10 and the heavy-chain variable region (VH) from antigold antibody A14P-b2 were amplified from plasmids pUTE[27] and pRAFHL,[13] respectively, by a polymerase chain reaction. DNA cassettes encoding the linker sequences were chemically synthesized. Gene fragments for the antibodies and each linker sequence were linked by an overlap extension polymerase chain reaction. The synthesized gene fragment of each BsAb was digested with the restriction enzymes *Hin*dIII and *Sac*II, and the resulting fragments were gel purified after electrophoresis and then ligated into expression vector pRA (designated as pRABsAb).

Table 1. Linker Sequences of BsAb's[a]

linker	amino acid sequence
PT21	$(PT)_3T(PT)_3T(PT)_2PST$
GR31	$GSG(GGGS)_2(GGGSE)_2(GGGS)_2GS$
diabody	GGGGS

[a] GR31 and PT21 linkers were engineered from a glycine-rich region of g3p from bacteriophage fd and a proline-rich region of *C. fimi* xylanase as templates.

Preparation of Antibodies by Means of a Refolding System. BsAb's and HyHEL10 scFv were prepared by means of a bacterial expression system similar to that described previously.[27] *Escherichia coli* strain BL21 (DE3) transformed with the expression vectors was cultured in 2 × YT medium containing 100 μg/mL ampicillin. Expression of the gene products was induced in the presence of 1 mM isopropylthiogalactoside. The cultures were harvested 16 h after induction. The gene products were collected as an insoluble inclusion body by centrifugation (13 000*g*, 30 min) after sonication of the bacteria. The inclusion body was solubilized in 6 M guanidine hydrochloride (Gdm-HCl) denaturant and then purified by metal chelate affinity chromatography on His-Bind resin (Novagen, Madison, WI). The denatured antibodies were refolded by stepwise dialysis. Briefly, Gdm-HCl was removed from the denatured antibody solution by dialysis (from 6 M Gdm-HCl to 3, 2, 1, 0.5, or 0 M) at 4 °C. The refolded antibodies were purified by size-exclusion chromatography on a Superdex 200pg column (GE Healthcare), and the monomer fraction was collected.

Kinetic Analysis of the BsAb−Lysozyme Interaction. The binding activity was measured by means of surface plasmon resonance (SPR). Hen egg lysozyme was purchased from Seikagaku-Kogyo Inc. (Tokyo, Japan). Lysozyme was immobilized on a CM5 sensor chip (GE Healthcare) by means of NHS/EDC chemistry in accordance with the chip manufacturer's protocol. The binding of BsAb to lysozyme was analyzed with a Biacore 2000 instrument (GE Healthcare) at a flow rate of 20 μL/min in phosphate-buffered saline containing 0.1% Tween 20. The kinetic parameters in a 1:1 binding model were determined with Biaevaluation 3.0 software (GE Healthcare).

Calculation of the Antigen-Binding Capacity of BsAb on a Gold Surface. Gold sensor chips from an SIA Kit Au (GE Healthcare) were cleaned with piranha solution (3:1 H_2SO_4/H_2O_2). Before the binding-capacity assay, the chips were subjected to a running buffer (phosphate-buffered saline containing 0.1% Tween 20) for 1 h. Treatment with the buffer containing the surfactant was crucial to blocking the nonspecific adsorption of lysozyme. The binding of BsAb to the gold surface and lysozyme was analyzed with a Biacore 2000 instrument (GE Healthcare). The nonspecific adsorption of lysozyme was checked after BsAb was dissociated from the sensor chip with 50 mM NaOH. The amount of lysozyme immobilized by BsAb was determined by subtracting the amount of nonspecifically adsorbed lysozyme from the total amount of lysozyme bound on the gold surface.

The SPR response (in response units, RU) is proportional to the protein mass concentration at a surface.[28] The amounts of immobilized BsAb and lysozyme were determined from RU values normalized by the respective molecular weights of the proteins. To evaluate the biosensing performance, we calculated the antigen-binding capacity of the BsAb's on the gold surface as the ratio of the amount of immobilized lysozyme to the amount of immobilized BsAb as follows

$$\text{binding capacity } (\%) = \frac{R_{\text{lysozyme}}/M_{w_{\text{lysozyme}}}}{R_{\text{BsAb}}/M_{w_{\text{BsAb}}}} \quad (1)$$

dx.doi.org/10.1021/la2006259 |*Langmuir* 2011, 27, 9656–9661

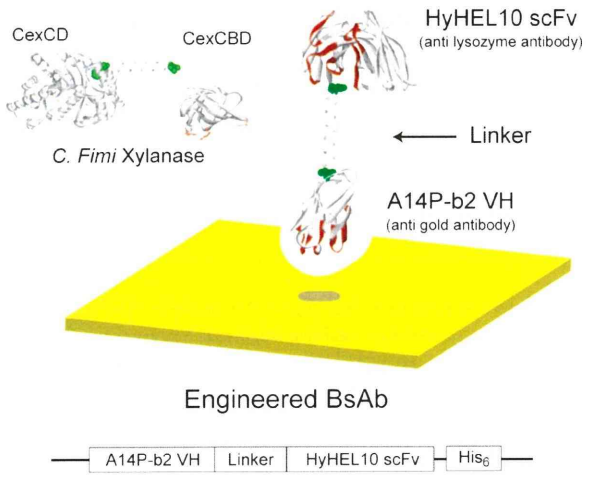

Figure 1. Schematic representation of an engineered bispecific antibody (BsAb) with a modular structure. The structures of HyHEL10 scFv and A14P-b2 VH were generated with Protein Data Bank code 1C08 and homology modeled coordinates,[36] respectively. CPK representations of the C-terminal end of A14P-b2, and the N-terminal end of HyHEL10 scFv are shown in green. Complementarity-determining regions of antibodies are shown in red. The inset shows the modular structure of *C. fimi* xylanase (Cex). The catalytic domain (CexCD) and the cellulose-binding domain (CexCBD) were modeled with Protein Data Bank codes 2EXO and 1EXG, respectively.

where R is the immobilized amount (in RU) and M_w is the molecular weight of bound protein.

RESULTS AND DISCUSSION

Design and Preparation of BsAb's. We developed a strategy for the design of BsAb's with modular structures consisting of an antigold antibody (A14P-b2), an antilysozyme antibody (HyHEL10), and one of three linker regions that connected the two antibody domains (Figure 1). To obtain a rigid linker, a flexible linker, and a short linker, we chose two naturally occurring proteins (a bacterial cellulase and filamentous bacteriophage fd coat protein g3p) and an artificial antibody fragment (diabody).

The three kinds of BsAb's (BsAb PT21, BsAb GR31, and diabody) were genetically engineered and prepared in an *E. coli* expression system with in vitro refolding. The diabody was obtained without high-molecular-weight aggregates, whereas aggregates of BsAb PT21 and BsAb GR31 were produced during the refolding step. The aggregates were removed by size-exclusion chromatography (Figure 2). Monomeric BsAb's with GR31 and PT21 linkers were obtained in final yields of 15 and 35 μg from 1 L culture, respectively. The relatively low yields are probably due to their long linker sequences. Improvement of the preparation such as the use of mammalian expression system should be the next issue to be addressed for further practical application.

The binding of BsAb's to lysozyme was analyzed by SPR (Supporting Information Figure S1)). The K_D values for BsAb PT21, BsAb GR31, diabody, and HyHEL10 scFv were 3.2, 0.79, 3.2, and 1.3 nM, respectively. The affinities of BsAb's were comparable to that of HyHEL10 scFv, indicating that neither of the long linkers attached at the N terminus of HyHEL10 scFv hindered binding to lysozyme. The specificity of the gold surface

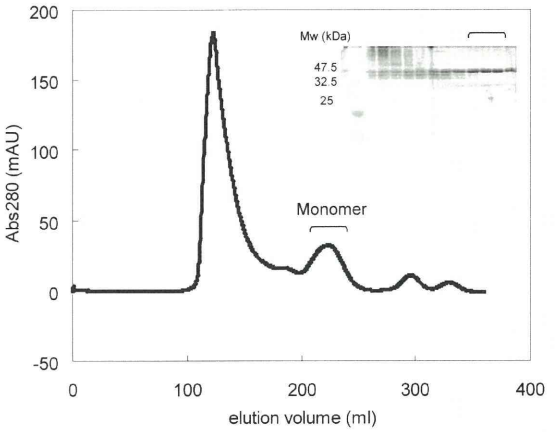

Figure 2. Size-exclusion chromatogram of BsAb PT21 prepared by means of a refolding system. The refolded BsAb was purified on a Superdex200pg column. The purity and uniformity were verified by nonreducing SDS-PAGE (inset). The monomer fraction of the BsAb was collected from the 210 to 240 mL fraction.

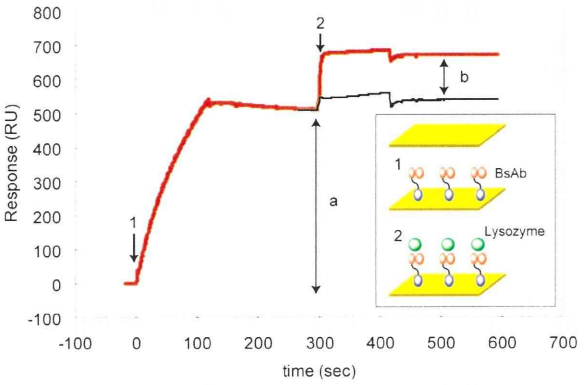

Figure 3. SPR sensorgram for the simultaneous binding of BsAb GR31 to a gold surface and to lysozyme. Arrows indicate the injection of BsAb (arrow 1) and lysozyme (arrow 2) at concentrations of 380 and 650 nM, respectively. The inset is a schematic diagram of the experiment showing the immobilization of lysozyme via BsAb on the gold surface. The amount of immobilized BsAb (double-headed arrow a) was obtained from the RU value just before the injection of lysozyme. The amount of lysozyme immobilized by BsAb (double-headed arrow b) was obtained by subtracting the amount of nonspecifically adsorbed lysozyme (curve in black) after lysozyme injection.

was confirmed by the immunostaining of six different metals (Supporting Information Figure S2). The refolded BsAb discriminated gold from other metals, including platinum, palladium, silver, aluminum, and tungsten, demonstrating the high affinity and specificity conferred on the BsAb.

Lysozyme Immobilization via BsAb's Immobilized on a Gold Surface. We measured the simultaneous binding of BsAb's to a gold surface and lysozyme by SPR; the sensorgram for BsAb GR31 is shown in Figure 3. Injection of the BsAb produced a clear SPR response, indicating tight binding to the gold sensor chip (arrow 1 in Figure 3); the K_D of BsAb GR31 was calculated to be 8.7 nM by curve fitting. When lysozyme was injected after the SPR response stabilized (arrow 2 in Figure 3), the added lysozyme was also captured on the BsAb-coated sensor chip.

dx.doi.org/10.1021/la2006259 |*Langmuir* 2011, 27, 9656–9661

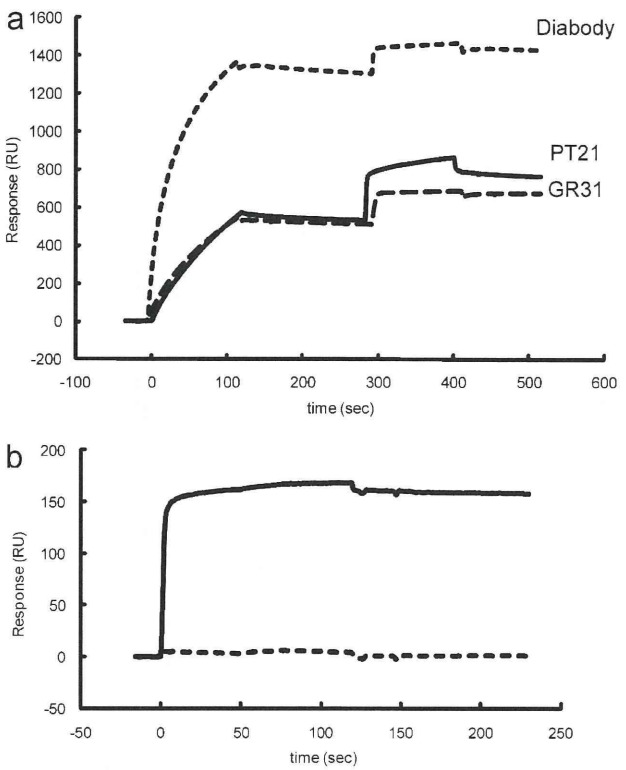

Figure 4. (a) SPR sensorgrams for the binding of BsAb PT21 (—), BsAb GR31 (---), and the diabody (· · ·) to the gold surface and to lysozyme. The BsAb's and lysozyme were injected at concentrations of 380 and 650 nM, respectively. (b) Lysozyme binding by HyHEL10 scFv immobilized on a CM5 sensor chip. The HyHEL10 scFv was immobilized at a density of 494 RU. Lysozyme was injected at a concentration of 650 nM. The experiment was performed under the conditions used for the BsAb's. The dotted line shows the nonspecific adsorption of lysozyme in a reference flow cell.

Note that before the SPR test the gold surface had been blocked with 0.1% Tween 20 to minimize the nonspecific adsorption of proteins. The surfactant prevented the adsorption of lysozyme but did not affect the interaction of BsAb's with both gold and lysozyme (Supporting Information Figures S1 and S3). Only a slight increase in RU due to the nonspecific adsorption of lysozyme was observed in the absence of BsAb (Figure 3, black curve). The amount of lysozyme immobilized by each BsAb was obtained by subtracting the amount of nonspecifically adsorbed lysozyme from the RU value after lysozyme injection. The SPR sensorgrams for the binding of lysozyme by the three kinds of BsAb's clearly demonstrate binding to the gold surface and the stacking of lysozyme (Figure 4). We also observed the differences in the BsAb binding on the gold surface. Lesser responses of GR31 and PT21 were probably due to their refolding efficiencies that reduced the effective concentrations of active gold-binding domains. Judging from the analysis of the interaction between BsAb's and lysozyme (Supporting Information Figure S1), the antilysozyme antibody domains of BsAb's were well refolded and capable of lysozyme-binding activity.

To evaluate the biosensing performance quantitatively (i.e., the retention of binding activity on the gold surface), we determined the antigen-binding capacity of the BsAb's immobilized on the gold surface. The antigen-binding capacity is given by the ratio of the amount of immobilized antigen to the amount of immobilized BsAb; the immobilized amounts were calculated from the RU values of lysozyme and BsAb normalized by their respective molecular weights. BsAb PT21 showed the highest antigen-binding capacity (up to 82%), followed by BsAb GR31 (66%) and the diabody (22%) (Figure 4 and Table 2). Although PT21 and GR31 have fewer active gold-binding domains than the diabody, the PT21 and GR31 adsorbed on the gold surface showed higher antigen-binding capacities than that of the diabody in spite of their lower refolding efficiencies. Although we previously confirmed that the diabody functions as a biointerface molecule that allows the specific accumulation of lysozyme onto patterned gold spots,[13] the results obtained here indicate that approximately 80% of the immobilized diabody lost binding activity on the gold surface. We assumed that the adsorbed proteins underwent some degree of structural deformation and that the five-residue linker of the diabody was not sufficiently long to completely separate the lysozyme-binding domain from the surface. A comparison between the results for the BsAb's with long linkers (PT21 and GR31) and the results for the diabody suggested that the higher antigen-binding capacities of the former were due to the elongation of the linker, which separated the sensing domain from the gold surface.

Table 2. Quantitative Analysis of the Biosensing Performance of BsAb's[a]

antibody	immobilized antibody (RU)	immobilized lysozyme (RU)	antigen-binding capacity (%)
BsAB PT21	488 ± 43	136 ± 6	82 ± 4
BsAb GR31	608 ± 118	136 ± 27	66 ± 9
diabody	1352 ± 38	84 ± 21	22 ± 6
HyHEL10 scFv	494	160	59

[a] The antigen-binding capacity was calculated from the amounts of immobilized antibody and antigen. The data are the means ± S.D.

We also found that the activity of the BsAb's depended on whether the linker was rigid or flexible. The PT21 linker derived from a cellulase, which contains multiple proline and threonine residues, conferred a higher antigen-binding capacity than did the glycine-rich linker from fd phage g3p (BsAb GR31). This result suggests that a rigid structure was more effective at retaining the binding activity. Considering that the linker regions of many cellulases that function on solid phases have evolved to contain proline-rich sequences,[24] the rigid structure must be necessary for maintaining the proper orientation of the functional domain of cellulases. It is interesting that the necessity of a rigid linker was extended to a BsAb with a cellulose-derived linker designed to function on the gold surface of a biosensing device.

How did the proline- and threonine-rich linker improve the antigen-binding capacity? We suggest that both the linker shape and the orientation of the linker with respect to the gold-binding region were responsible for retention of the binding activity. Small-angle X-ray scattering studies of cellulases have indicated that they have an extended "tadpole shape,"[22,23] which favorably orients the two domains for the expression of their respective functions. The binding site of an antibody (known as the complementarity-determining region) is positioned at the opposite end of the C terminus to which the PT linker is fused (Figure 1). Therefore, a possible explanation of the improvement that we observed is that the long, rigid linker effectively oriented the antigen-binding domain and separated it from the gold surface.

dx.doi.org/10.1021/la2006259 |Langmuir 2011, 27, 9656–9661

Similarly, the importance of the chain conformation has been suggested in chemical cross-linking,[29] in which the activities of immobilized antibodies are not a direct function of the spacer length. In summary, we concluded that the optimum linker for BsAb must be long enough to separate the sensing domain from the surface (20 amino acid residues in this study) and must have a rather rigid structure.

Comparison of BsAb-Based Immobilization with Conventional Immobilization Methods. BsAb-based immobilization provides a novel and effective alternative to conventional methods such as physical adsorption or NHS/EDC chemistry. The physical adsorption of proteins often results in a loss of their activity. For instance, Butler et al. reported that <3.0% of adsorbed antibodies capture antigens on polystyrene surfaces.[5] In contrast, the BsAb's that we designed retained their binding abilities on the gold surface, with a maximum antigen-binding capacity of 82%. NHS/EDC chemistry, in which the protein of interest is coupled via primary amino groups, has been widely used for immobilization. For comparison with this conventional method, we immobilized HyHEL10 scFv on a CM5 sensor chip by amine coupling and determined the antigen-binding capacity. The antigen-binding capacity of the amino-coupled HyHEL10 scFv was calculated to be 59% (Figure 4b, Table 2); this indicated that BsAb-based immobilization afforded an antigen-binding capacity comparable or superior to that obtained by means of NHS/EDC chemistry.

Furthermore, BsAb-based immobilization has an advantage over conventional methods in that direct immobilization on a solid surface can be accomplished with no chemical modification of the surface. This method can be applied to material surfaces that are difficult to modify covalently as long as a binder with affinity for the material can be obtained. We previously reported the in vitro selection of antibodies for various material surfaces such as biodegradable plastic[30] and ZnO,[31] and we have used these antibodies to perform antibody-based surface modification[32] and antigen biosensing.[33] In principle, the combination of the selection technology with the molecular design discussed here enables us to generate biointerface molecules that are specific to any material surface. An antibody that folds into a specific structure has a high affinity and specificity for its target surface, without the need for affinity improvement that is often required for peptides,[34,35] and is well suited to act as a high-affinity binder applicable to other surfaces of sensor devices.

CONCLUSIONS

By taking advantage of antibody−antigen recognition and the modular structures of some naturally occurring proteins, we generated BsAb's that functioned as biointerface molecules between a biomolecule and a material surface. A BsAb with a cellulase-derived linker retained its activity on a gold surface. The correlation of the activity and linker shape demonstrated that a modular structure with two distinct domains and a long, rigid linker provided the optimum antigen-binding capacity. This BsAb is a promising candidate for biosensing molecules and building blocks for nanoscale fabrication.

ASSOCIATED CONTENT

Supporting Information. Description of the SPR analysis of the BsAb−lysozyme interaction, the metal specificity of an antigold BsAb, and adsorption experiments. This material is available free of charge via the Internet at http://pubs.acs.org.

AUTHOR INFORMATION

Corresponding Author

*Tel: +81-22-795-7274. Fax: +81-22-795-6164. E-mail: kmiz@kuma.che.tohoku.ac.jp.

ACKNOWLEDGMENT

This work was supported in part by a grant-in-aid for scientific research S to I.K. from the Japan Society for the Promotion of Science (JSPS), Japan.

REFERENCES

(1) Scheller, F. W.; Wollenberger, U.; Warsinke, A.; Lisdat, F. Research and development in biosensors. *Curr. Opin. Biotechnol.* **2001**, *12*, 35–40.

(2) Boldicke, T.; Struck, F.; Schaper, F.; Tegge, W.; Sobek, H.; Villbrandt, B.; Lankenau, P.; Bocher, M. A new peptide-affinity tag for the detection and affinity purification of recombinant proteins with a monoclonal antibody. *J. Immunol. Methods* **2000**, *240*, 165–183.

(3) Peruski, A. H.; Peruski, L. F., Jr. Immunological methods for detection and identification of infectious disease and biological warfare agents. *Clin. Diagn. Lab. Immunol.* **2003**, *10*, 506–513.

(4) Huang, L.; Reekmans, G.; Saerens, D.; Friedt, J. M.; Frederix, F.; Francis, L.; Muyldermans, S.; Campitelli, A.; Van Hoof, C. Prostate-specific antigen immunosensing based on mixed self-assembled monolayers, camel antibodies and colloidal gold enhanced sandwich assays. *Biosens. Bioelectron.* **2005**, *21*, 483–490.

(5) Butler, J. E.; Ni, L.; Nessler, R.; Joshi, K. S.; Suter, M.; Rosenberg, B.; Chang, J.; Brown, W. R.; Cantarero, L. A. The physical and functional behavior of capture antibodies adsorbed on polystyrene. *J. Immunol. Methods* **1992**, *150*, 77–90.

(6) Butler, J. E.; Ni, L.; Brown, W. R.; Joshi, K. S.; Chang, J.; Rosenberg, B.; Voss, E. W., Jr. The immunochemistry of sandwich ELISAs—VI. Greater than 90% of monoclonal and 75% of polyclonal anti-fluorescyl capture antibodies (CAbs) are denatured by passive adsorption. *Mol. Immunol.* **1993**, *30*, 1165–1175.

(7) Dietrich, C.; Boscheinen, O.; Scharf, K. D.; Schmitt, L.; Tampé, R. Functional immobilization of a DNA-binding protein at a membrane interface via histidine tag and synthetic chelator lipids. *Biochemistry* **1996**, *35*, 1100–1105.

(8) Evan, G. I.; Lewis, G. K.; Ramsay, G.; Bishop, J. M. Isolation of monoclonal antibodies specific for human c-myc proto-oncogene product. *Mol. Cell. Biol.* **1985**, *5*, 3610–3616.

(9) Knappik, A.; Plückthun, A. An improved affinity tag based on the FLAG peptide for the detection and purification of recombinant antibody fragments. *Biotechniques* **1994**, *17*, 754–761.

(10) Gaj, T.; Meyer, S. C.; Ghosh, I. *Protein Expr. Purif.* **2007**, *56*, 54–61.

(11) Tajima, N.; Takai, M.; Ishihara, K. Significance of antibody orientation unraveled: well-oriented antibodies recorded high affinity. *Anal. Chem.* **2011**, *83*, 1969–1976.

(12) Rusmini, F.; Zhong, Z.; Feijen, J. Protein immobilization strategies for protein biochips. *Biomacromolecules* **2007**, *8*, 1775–1789.

(13) Watanabe, H.; Nakanishi, T.; Umetsu, M.; Kumagai, I. Human anti-gold antibodies: Biofunctionalization of gold nanoparticles and surfaces with anti-gold antibodies. *J. Biol. Chem.* **2008**, *283*, 36031–36038.

(14) Smith-Gill, S. J.; Lavoie, T. B.; Mainhart, C. R. Antigenic regions defined by monoclonal antibodies correspond to structural domains of avian lysozyme. *J. Immunol.* **1984**, *133*, 384–393.

(15) Hilden, L.; Johansson, G. Recent developments on cellulases and carbohydrate-binding modules with cellulose affinity. *Biotechnol. Lett.* **2004**, *26*, 1683–1693.

(16) Lynd, L. R.; Weimer, P. J.; van Zyl, W. H.; Pretorius, I. S. Microbial cellulose utilization: fundamentals and biotechnology. *Microbiol. Mol. Biol. Rev.* **2002**, *66*, 506–577.

(17) Riechmann, L.; Holliger, P. The C-terminal domain of TolA is the coreceptor for filamentous phage infection of *E. coli*. *Cell* **1997**, *90*, 351–360.

(18) Hudson, P. J.; Souriau, C. Engineered antibodies. *Nat. Med.* **2003**, *9*, 129–134.
(19) Carvalho, A. L.; Goyal, A.; Prates, J. A.; Bolam, D. N.; Gilbert, H. J.; Pires, V. M.; Ferreira, L. M.; Planas, A.; Romao, M. J.; Fontes, C. M. The family 11 carbohydrate-binding module of *Clostridium thermocellum* Lic26A-Cel5E accommodates beta-1,4- and beta-1,3−1,4-mixed linked glucans at a single binding site. *J. Biol. Chem.* **2004**, *279*, 34785–34793.
(20) Itoh, Y.; Kawase, T.; Nikaidou, N.; Fukada, H.; Mitsutomi, M.; Watanabe, T.; Itoh, Y. Functional analysis of the chitin-binding domain of a family 19 Chitinase from *Streptomyces griseus* HUT6037: substrate-binding affinity and cis-dominant increase of antifungal function. *Biosci. Biotechnol. Biochem.* **2002**, *66*, 1084–1092.
(21) Kasuya, K.; Ohura, T.; Masuda, K.; Doi, Y. Substrate and binding specificities of bacterial polyhydroxybutyrate depolymerases. *Int. J. Biol. Macromol.* **1999**, *24*, 329–336.
(22) Shen, H.; Schmuck, M.; Pilz, I.; Gilkes, N. R.; Kilburn, D. G.; Miller, R. C., Jr.; Warren, R. A. Deletion of the linker connecting the catalytic and cellulose-binding domains of endoglucanase A (CenA) of *Cellulomonas fimi* alters its conformation and catalytic activity. *J. Biol. Chem.* **1991**, *266*, 11335–11340.
(23) Receveur, V.; Czjzek, M.; Schulein, M.; Panine, P.; Henrissat, B. Dimension, shape, and conformational flexibility of a two domain fungal cellulase in solution probed by small angle X-ray scattering. *J. Biol. Chem.* **2002**, *277*, 40887–40892.
(24) Gilkes, N. R.; Henrissat, B.; Kilburn, D. G.; Miller, R. C., Jr.; Warren, R. A. Domains in microbial beta-1, 4-glycanases: sequence conservation, function, and enzyme families. *Microbiol. Rev.* **1991**, *55*, 303–315.
(25) Ji, Q.; Vincken, J. P.; Suurs, L. C.; Visser, R. G. Microbial starch-binding domains as a tool for targeting proteins to granules during starch biosynthesis. *Plant. Mol. Biol.* **2003**, *51*, 789–801.
(26) Kortt, A. A.; Dolezal, O.; Power, B. E.; Hudson, P. J. Dimeric and trimeric antibodies: high avidity scFvs for cancer targeting. *Biomol. Eng.* **2001**, *18*, 95–108.
(27) Umetsu, M.; Tsumoto, K.; Hara, M.; Ashish, K.; Goda, S.; Adschiri, T.; Kumagai, I. How additives influence the refolding of immunoglobulin-folded proteins in a stepwise dialysis system. Spectroscopic evidence for highly efficient refolding of a single-chain Fv fragment. *J. Biol. Chem.* **2003**, *278*, 8979–8987.
(28) Karlsson, R.; Michaelsson, A.; Mattsson, L. Kinetic analysis of monoclonal antibody-antigen interactions with a new biosensor based analytical system. *J. Immunol. Methods* **1991**, *145*, 229–240.
(29) Cao, T.; Wang, A.; Liang, X.; Tang, H.; Auner, G. W.; Salley, S. O.; Ng., K. Y. Investigation of spacer length effect on immobilized Escherichia coli pili-antibody molecular recognition by AFM. *Biotechnol. Bioeng.* **2007**, *98*, 1109–1122.
(30) Watanabe, H.; Tsumoto, K.; Taguchi, S.; Yamashita, K.; Doi, Y.; Nishimiya, Y.; Kondo, H.; Umetsu, M.; Kumagai, I. A human antibody fragment with high affinity for biodegradable polymer film. *Bioconjugate Chem.* **2007**, *18*, 645–651.
(31) Hattori, T.; Umetsu, M.; Nakanishi, T.; Togashi, T.; Yokoo, N.; Abe, H.; Ohara, S.; Adschiri, T.; Kumagai, I. High affinity anti-inorganic material antibody generation by integrating graft and evolution technologies: potential of antibodies as biointerface molecules. *J. Biol. Chem.* **2010**, *285*, 7784–7793.
(32) Umetsu, M.; Hattori, T.; Kikuchi, S.; Muto, I.; Nakanishi, T.; Watanabe, H.; Kumagai, I. Nanoparticles with affinity for biopolymer: Bioassisted room-temperature selective multistacking of inorganic particles on biopolymer film. *J. Mater. Res.* **2008**, *23*, 3241–3246.
(33) Ibii, T.; Kaieda, M.; Hatakeyama, S.; Shiotsuka, H.; Watanabe, H.; Umetsu, M.; Kumagai, I.; Imamura, T. Direct immobilization of gold-binding antibody fragments for immunosensor applications. *Anal. Chem.* **2010**, *82*, 4229–4235.
(34) Brown, S. Metal-recognition by repeating polypeptides. *Nat. Biotechnol.* **1997**, *15*, 269–272.
(35) Tamerler, C.; Oren, E. E.; Duman, M.; Venkatasubramanian, E.; Sarikaya, M. Adsorption kinetics of an engineered gold binding peptide by surface plasmon resonance spectroscopy and a quartz crystal microbalance. *Langmuir* **2006**, *22*, 7712–7718.
(36) Schwede, T.; Kopp, J.; Guex, N.; Peitsch, M. C. SWISS-MODEL: An automated protein homology-modeling server. *Nucleic Acids Res.* **2003**, *31*, 3381–3385.

THE JOURNAL OF BIOLOGICAL CHEMISTRY VOL. 286, NO. 3, pp. 1812–1818, January 21, 2011

Cytotoxic Enhancement of a Bispecific Diabody by Format Conversion to Tandem Single-chain Variable Fragment (taFv)

*THE CASE OF THE hEx3 DIABODY**

Received for publication, August 6, 2010, and in revised form, October 12, 2010 Published, JBC Papers in Press, November 19, 2010, DOI 10.1074/jbc.M110.172957

Ryutaro Asano, Keiko Ikoma, Ippei Shimomura, Shintaro Taki, Takeshi Nakanishi, Mitsuo Umetsu, and Izumi Kumagai[1]

From the Department of Biomolecular Engineering, Graduate School of Engineering, Tohoku University, Sendai 980-8579, Japan

Diabodies (Dbs) and tandem single-chain variable fragments (taFv) are the most widely used recombinant formats for constructing small bispecific antibodies. However, only a few studies have compared these formats, and none have discussed their binding kinetics and cross-linking ability. We previously reported the usefulness for cancer immunotherapy of a humanized bispecific Db (hEx3-Db) and its single-chain format (hEx3-scDb) that target epidermal growth factor receptor and CD3. Here, we converted hEx3-Db into a taFv format to investigate how format affects the function of a small bispecific antibody; our investigation included a cytotoxicity assay, surface plasmon resonance spectroscopy, thermodynamic analysis, and flow cytometry. The prepared taFv (hEx3-taFv) showed an enhanced cytotoxicity, which may be attributable to a structural superiority to the diabody format in cross-linking target cells but not to differences in the binding affinities of the formats. Comparable cross-linking ability for soluble antigens was observed among hEx3-Db, hEx3-scDb, and hEx3-taFv with surface plasmon resonance spectroscopy. Furthermore, drastic increases in cytotoxicity were found in the dimeric form of hEx3-taFv, especially when the two hEx3-taFv were covalently linked. Our results show that converting the format of small bispecific antibodies can improve their function. In particular, for small bispecific antibodies that target tumor and immune cells, a functional orientation that avoids steric hindrance in cross-linking two target cells may be important in enhancing the growth inhibition effect.

Bispecific antibodies (BsAbs)[2] are recombinant antibodies that can bind to two different antigenic epitopes. Bispecificity can be used in cancer immunotherapy to cross-link tumor cells to immune cells such as cytotoxic T cells, natural killer cells, and macrophages. This cross-linking accelerates the destruction of the tumor cells by the immune cells, so that the high potency of BsAb may translate into improved antitumor therapy and lower treatment costs by decreasing the necessary doses (1, 2). However, the use of BsAbs in clinical studies has been hampered by difficulties in producing them on a large scale. Conventional chemical conjugation has been used, but the quality of the antibodies produced is inconsistent (3). The production of BsAbs by somatic fusion of two hybridomas to form a quadroma yields BsAbs of more consistent quality but results in the formation of various chain-shuffled antibodies; for instance, 10 different antibodies can be generated after random association of two heavy and two light chains (4, 5).

Advances in recombinant technology have made it feasible to generate small recombinant BsAbs constructed from two different variable antibody fragments, such as variable fragments (Fv) and single-chain Fv (scFv). These recombinant BsAbs include bispecific diabodies (Dbs) (6), single-chain diabodies (scDbs) (7), tandem scFv (taFv) (8), and minibodies (dimeric scDb-CH3 fusion proteins) (9). Compared with classic BsAbs prepared through chemical conjugation or quadroma production, small BsAbs have a convenient size for rapid tissue penetration and high target retention (10, 11). Although their rapid blood clearance and monovalency may limit therapeutic applications for small BsAbs, the length and amino acid composition of the linkers can be engineered to allow small BsAbs to assemble into multimers, such as tandem scDbs (12) and bispecific Db tetramers (tetrabodies) (13), with higher molecular weights and bivalency for the target antigens.

Among these small recombinant BsAbs, Dbs and taFv are the most widely used formats in constructing BsAbs, and their features and structural differences have been reviewed (2, 5, 14). In brief, Dbs can generally be produced in bacteria as soluble proteins, which is an important advantage over taFv. Although inactive homodimers can be produced along with the active heterodimers, homodimer formation can be avoided by connecting the two hetero-scFv fragments with an additional middle linker (*i.e.* by making scDbs). In contrast, taFv can be produced as a single species. Furthermore, the two binding sites in a taFv can rotate freely, and their axes can be kinked, which might facilitate simultaneous binding of two antigen epitopes juxtaposed on two different cell surfaces.

* This work was supported by grants-in-aid for scientific research from the Ministry of Education, Science, Sports, and Culture of Japan (to R. A. and I. K.) and by grants from the New Energy and Industrial Technology Development Organization of Japan. This work was also supported by the Program for Promotion of Fundamental Studies in Health Sciences of the National Institute of Biomedical Innovation.

[1] To whom correspondence should be addressed: Aoba 6-6-11-606, Aramaki, Aoba-ku, Sendai 980-8579, Japan. Fax: 81-22-795-6164; E-mail: kmiz@kuma.che.tohoku.ac.jp.

[2] The abbreviations used are: BsAb, bispecific antibody; Db, diabody; EGFR, EGF receptor; Fv, variable fragment(s); HRV3C, human rhinovirus 3C; MTS, 3-(4,5-dimethylthiazole-2-yl)-5-(3-carboxymethoxyphenyl)-2-(4-sulfophenyl)-2*H*-tetrazolium inner salt; scDb, single-chain diabody; scFv, single-chain Fv(s); sEGFR, soluble EGFR; SPR, surface plasmon resonance; T-LAK, lymphokine-activated killer cells with the T-cell phenotype; taFv, tandem scFv(s).

To date, however, there have been few reports presenting comparative analyses of bispecific Dbs and taFv consisting of identical valuable fragments (15) and no reports that discuss differences in binding kinetics and cross-linking ability. There have also been no reports on the influence of format on the cytotoxicity of small BsAbs that retarget immune cells against tumor cells. We previously reported the marked antitumor activity *in vitro* and *in vivo* of a humanized bispecific Db targeting EGF receptor (EGFR) and CD3 (hEx3-Db) (16). Here, we converted the hEx3-Db into a taFv format to discuss in detail the influence of BsAb fusion format on function.

For a comparative analysis, it is desirable to prepare high-quality small BsAbs using the same host-vector system for both samples. In addition, the peptide tag usually required for purification may affect function. We previously developed a preparation method for high quality, tag-free small BsAbs using the Fc fusion format and protease digestion (17). In this study, we applied this method for the preparation of a taFv format of hEx3 (hEx3-taFv). Interestingly, the resulting hEx3-taFv showed an enhanced cytotoxicity, which may be attributable to a structural superiority to the diabody format in cross-linking between target cells rather than to a difference in binding affinity. Furthermore, drastic increases in cytotoxicity were found in the dimeric form, especially when two hEx3-taFv were covalently linked. Our results show that the effectiveness of small BsAbs targeting tumor and immune cells could be improved by changing their recombinant formats.

EXPERIMENTAL PROCEDURES

Preparation of Recombinant BsAbs—We previously developed a method for the preparation of tag-free small BsAbs using the Fc fusion format and a restriction protease, and we successfully prepared hEx3-Db and hEx3-scDb in their Fc fusion formats, hEx3-Db-3C-Fc and hEx3-scDb-3C-Fc, respectively (17). In this study, we applied this method for the preparation of an hEx3-taFv dimer linked by a hinge region (hEx3-(taFv′)$_2$). To construct the gene for hEx3-taFv, humanized anti-EGFR scFv with a variable light-variable heavy domain orientation and humanized anti-CD3 scFv with a variable heavy-variable light domain orientation were joined via a GGGGS linker by overlap PCR. Then, the hEx3-taFv and the human IgG1 Fc region were connected via the recognition site (LEVLFQGP) for human rhinovirus 3C protease (HRV3C) in two different manners. For hEx3-taFv, the recognition site was inserted before the hinge region; for hEx3-(taFv′)$_2$, it was inserted after the hinge region. The gene constructs, hEx3-taFv-3C-Fc and hEx3-taFv′-3C-Fc, were inserted into pcDNA3.1/Neo mammalian expression vectors (Invitrogen). The leader peptide sequences for protein secretion were derived from mouse OKT3 IgG (18).

The methods for expression using CHO cells and purification have been described previously (17). In brief, IgG-like BsAbs of hEx3-taFv-3C-Fc and hEx3-taFv′-3C-Fc were first purified on a protein A column (GE Healthcare) and then digested by HRV3C protease fused to glutathione *S*-transferase (PreScission protease; GE Healthcare) according to the protocol described by the manufacturer. The protease was removed on a glutathione-Sepharose 4B column (GE Healthcare), and the flow-through was loaded on the protein A column again to remove the digested Fc and undigested Fc fusion protein. The presence of the BsAbs was confirmed by SDS-PAGE at each stage of purification.

Gel Filtration Chromatography—Gel filtration analysis with a Hiload Superdex 200-pg column (10/300; GE Healthcare) was used to evaluate the structure of the BsAbs. The column was equilibrated with PBS, and then 250 μl of purified BsAbs was applied to the column at a flow rate of 0.5 ml/min. For functional analyses, each BsAb solution was fractionated on a Hiload Superdex 200-pg column (26/60; GE Healthcare). The column was equilibrated with PBS, and then 5 ml of purified BsAbs was applied to the column at a flow rate of 2.5 ml/min.

In Vitro Growth Inhibition Assay—Lymphokine-activated killer cells with the T-cell phenotype (T-LAK) cells were induced as reported previously (19). In brief, peripheral blood mononuclear cells were cultured for 48 h at a density of 1×10^6 cells/ml in a medium supplemented with 100 IU/ml of recombinant human IL-2 (Shionogi Pharmaceutical Co., Osaka, Japan) in a culture flask (A/S Nunc, Roskilde, Denmark) that was precoated with anti-CD3 monoclonal antibody (10 μg/ml).

The *in vitro* growth inhibition of TFK-1 (human bile duct carcinoma) cells was assayed with a 3-(4,5-dimethylthiazole-2-yl)-5-(3-carboxymethoxyphenyl)-2-(4-sulfophenyl)-2*H*-tetrazolium inner salt (MTS) assay kit (CellTiter 96 AQueous Nonradioactive Cell Proliferation Assay; Promega, Madison, WI) as reported previously (19).

Surface Plasmon Resonance Spectroscopy—The interactions between soluble EGFR (sEGFR) and the BsAbs were analyzed by surface plasmon resonance (SPR) spectroscopy with a BIACORE 2000 (GE Healthcare). Methods for the expression and purification of sEGFR have been described previously (20). The sEGFR was immobilized on the cells in a CM5 sensor chip up to 2716 resonance units. Various concentrations of BsAbs in PBS with 0.005% Tween 20 were flowed over the sEGFR. The data were normalized by subtracting the response of a blank cell with blocking. BIAevaluation software (GE Healthcare) was used to analyze the data. Kinetic parameters were calculated by a global fitting analysis with the assumption of a 1:1 Langmuir binding model.

Isothermal Titration Calorimetry—Thermodynamic analyses of the interactions of BsAbs with sEGFR and CD3$\epsilon\gamma$ were performed by microtitration calorimetry using a VP-ITC from MicroCal, Inc. (Northampton, MA) (21). The methods for the expression and purification of CD3$\epsilon\gamma$ have been described previously (22). Each sample (1.5 μM in PBS, pH 7.2, 0.005% Tween 20) was placed in a calorimeter cell and titrated with 30 μM sEGFR in the same buffer; for CD3$\epsilon\gamma$, 1.25 μM hEx3 was titrated with 50 μM CD3$\epsilon\gamma$. The ligand solution was injected 25 times in 10-μl portions over a period of 15 s. Data acquisition and subsequent nonlinear regression analyses were done in terms of a simple binding model, using the MicroCal ORIGIN software package (version 5.0).

Confirmation of Cross-linking Ability—FITC-sEGFR was prepared with the fluorescein labeling kit NH2 (Dojindo Laboratories, Kumamoto, Japan) for confirmation of cross-linking between sEGFR and T-LAK cells. T-LAK cells (1×10^6) were

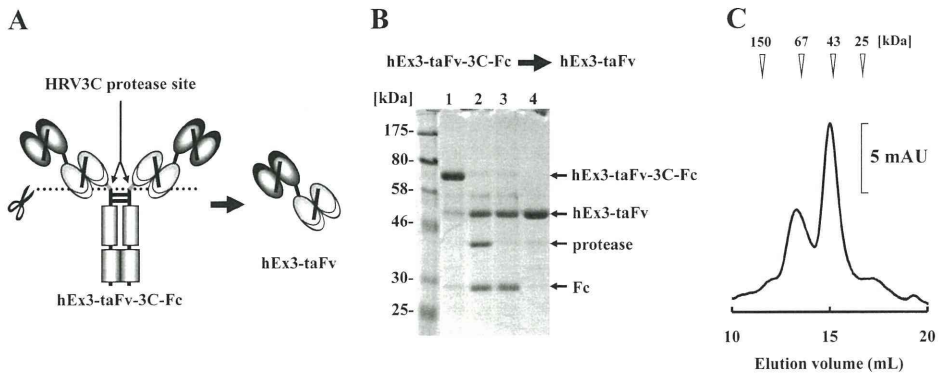

FIGURE 1. *A*, schematic illustration of the hEx3-taFv-3C-Fc fusion protein. The HRV3C protease cleavage site used for preparation of hEx3-taFv is indicated. *B*, reducing SDS-PAGE of each purification step in the preparation of hEx3-taFv from hEx3-taFv-3C-Fc. *Lane 1*, protein A chromatography-purified hEx3-taFv-3C-Fc; *lane 2*, after HRV3C protease digestion; *lane 3*, after removal of HRV3C protease by glutathione-Sepharose 4B chromatography; *lane 4*, purified hEx3-taFv after removal of the Fc region by protein A chromatography. *C*, gel filtration of purified hEx3-taFv. *mAU*, milliabsorbance unit.

incubated on ice with 400 pmol of each BsAb for 30 min. After a wash with PBS containing 0.1% NaN_3, they were exposed to 1 μg of FITC-sEGFR for 30 min on ice. The stained cells were analyzed by flow cytometry (FACSCalibur, Becton Dickinson, San Jose, CA) (16). To test the cross-linking between sEGFR and CD3$\epsilon\gamma$, 0.5 μM fractionated hEx3s in PBS with 0.005% Tween 20 were flowed over the sEGFR-immobilized sensor chip for 50 s. After PBS with 0.005% Tween 20 was flowed over the chip for 110 s, an excess of CD3$\epsilon\gamma$ was flowed for 50 s.

ELISA—BsAbs at the final concentration of 10 nM were co-cultured with T-LAK cells (5×10^4) in the presence or absence of overnight-adhered TFK-1 cells (5×10^3). After 12 h of co-culture, the supernatants were harvested and applied for ELISA with human IL-2 and interferon-γ ELISA Ready-SET-Go! (Bay Bioscience, Co., Ltd., Hyogo, Japan), following the manufacturer's instructions.

RESULTS

Preparation of hEx3 in a Tandem scFv Format—We previously reported the preparation of high quality hEx3-Db using the Fc fusion format (hEx3-Db-3C-Fc) and a restriction protease (17). To investigate the effects of BsAb formats on their functions, we prepared hEx3 in a tandem scFv format (hEx3-taFv) by applying the same method (Fig. 1*A*). The expressed hEx3-taFv-3C-Fcs were purified by protein A affinity chromatography and digested with glutathione *S*-transferase-fused HRV3C protease. The treated solution was loaded onto a glutathione-immobilized column followed by a protein A column to remove added protease and digested Fc. SDS-PAGE analysis of each purification step showed the successful preparation of hEx3-taFv from its Fc fusion format (Fig. 1*B*). Because two peaks corresponding to the monomers and dimers of hEx3-taFv were found in subsequent gel filtration chromatography (Fig. 1*C*), we used each fractionated hEx3-taFv for further analyses. The final yields of monomers and dimers were 1 mg and 0.5 mg/liter culture, respectively.

Effect of BsAb Format on Growth Inhibition—To evaluate the influence of the two BsAb formats on the inhibition of human carcinoma cell growth, we analyzed hEx3-Db and fractionated hEx3-taFv monomer with MTS. In the presence of T-LAK cells, the hEx3-taFv monomer inhibited cell growth more effectively than the hEx3-Db (Fig. 2*A*), suggesting that the tandem scFv format is structurally superior to the diabody format for hEx3. When peripheral blood mononuclear cells were applied as effector cells, the hEx3-taFv also inhibited more effectively than the hEx3-Db (Fig. 2*B*). For further confirmation of this superiority, we compared the growth inhibition effects of their IgG-like BsAb formats before digestion: hEx3-Db-3C-Fc and hEx3-taFv-3C-Fc. Both IgG-like BsAbs strongly inhibited the growth of TFK-1 cells even at a concentration of 0.1 pmol/ml, and the hEx3-taFv-3C-Fc, with a tandem scFv format, was also highly effective at a much lower concentration (Fig. 2*C*). The two small BsAb portions of the taFv format might contribute to this substantial difference. Thus, the activity of BsAbs can be enhanced by changing their structural formats.

Comparison of Binding Constants with SPR Spectroscopy and Thermodynamic Analysis—We previously reported that hEx3-Db has an effect similar to that of its single-chain form, hEx3-scDb (23, 24). To compare the growth inhibition effects and binding affinities among hEx3-Db, hEx3-scDb, and hEx3-taFv, we performed kinetic analyses for immobilized sEGFR by SPR imaging. Although hEx3-scDb showed the highest affinity for sEGFR, major differences among these three small BsAbs were not observed for any of the kinetic parameters (Table 1). Because the binding kinetics for CD3 were not determined, due to the inactivation of immobilized CD3 on a sensor chip, we performed thermodynamic analyses for sEGFR and CD3 by means of isothermal titration calorimetry. Whereas the K_A values for sEGFR were comparable to those found by SPR imaging for each small BsAb, the affinity for CD3 was 28× as great in hEx3-scDb and 9× as great in hEx3-taFv as in hEx3-Db. These results may indicate that the binding affinity of BsAbs, especially for effector cells, has little correlation with their growth inhibition effects, at least in hEx3 BsAbs.

Cross-linking Ability of Each BsAb—To investigate which factors contributed to the higher antitumor effects of hEx3-taFv, we examined the cross-linking ability of small BsAbs by flow cytometry and SPR spectroscopy. The multimeric form

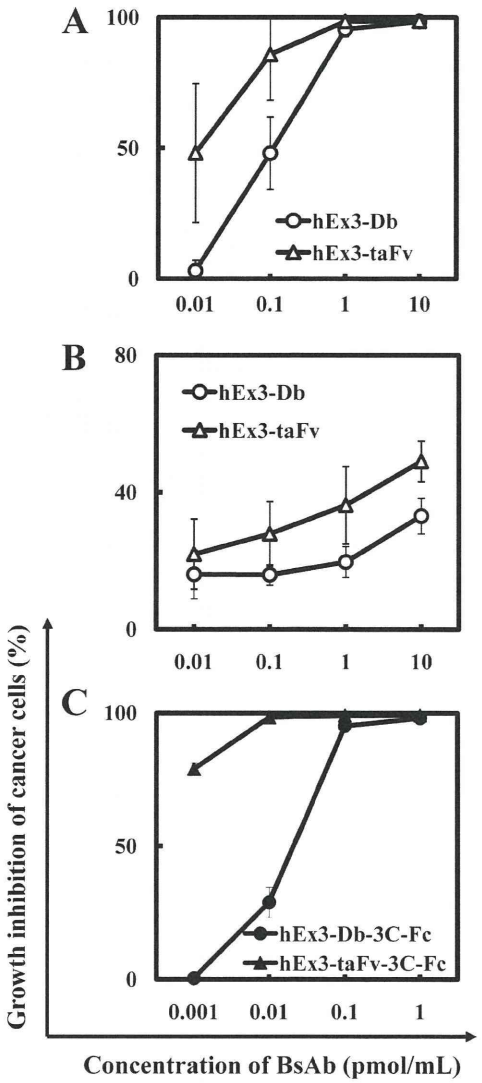

FIGURE 2. **Growth inhibition of EGFR-positive TFK-1 cells by each BsAb.** Comparison between small BsAb formats (*A* and *B*) and Fc fusion formats (*C*). BsAbs and T-LAK cells were added to TFK-1 cells at a ratio of 5 to 1 (*A* and *C*). BsAbs and peripheral blood mononuclear cells were added to TFK-1 cells at a ratio of 10:1. *B*, data are presented as the mean value ± S.D. and are representative of at least three independent experiments with similar results.

TABLE 1
Binding kinetics for sEGFR evaluated with surface plasmon resonance spectroscopy

	k_{on}	k_{off}	K_A
	$\times 10^5\ M^{-1}\ s^{-1}$	$\times 10^{-3}\ s^{-1}$	$\times 10^7\ M^{-1}$
hEx3-Db[a]	2.6	5.5	4.8
hEx3-scDb	1.9	5.4	3.6
hEx3-taFv	1.4	6.5	2.1

[a] Data from our previous report (22) are shown.

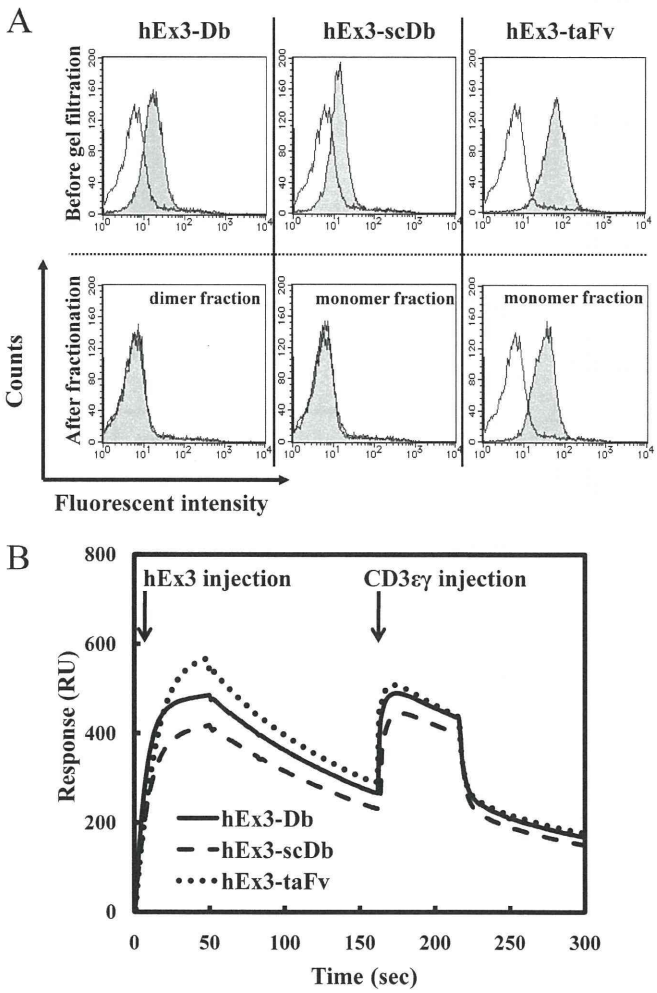

FIGURE 3. **Confirmation of cross-linking ability of small BsAbs.** *A*, in the flow cytometry analysis, T-LAK cells were incubated with PBS as a negative control (*open area*) or with each BsAb (*shaded area*), and incubation was followed by staining with FITC-sEGFR. Results for prepared BsAbs before gel filtration (*upper panels*) and for BsAbs fractionated by gel filtration (*lower panels*). *B*, in the surface plasmon resonance spectroscopy analysis, CD3εγ was injected after hEx3s were flowed over the sEGFR-immobilized sensor chip. *RU*, resonance units.

was observed not only in the prepared hEx3-taFv solution (Fig. 1*C*) but also in hEx3-Db (17) and hEx3-scDb (data not shown). In the unfractionated samples, all the BsAbs showed the ability to cross-link between T-LAK cells and sEGFR, and the most effective was hEx3-taFv (*upper panel*, Fig. 3*A*). In contrast, in the fractionated samples (dimer fraction for hEx3-Db, monomer fractions for hEx3-scDb and hEx3-taFv), only hEx3-taFv showed effective cross-linking ability (*lower panel*, Fig. 3*A*). Interestingly, no major differences in cross-linking ability for soluble antigens were observed between the small BsAbs in the SPR analyses (Fig. 3*B*). The flexibility of the taFv format might contribute to the avoidance of steric hindrance with other cell surface molecules in the cross-linking between target cells.

Effect of BsAb Format on Cytokine Production—To investigate whether the differences in cross-linking ability affect cytokine production from T-LAK cells, we analyzed the concentrations of IL-2 and IFN-γ in the culture supernatant of T-LAK cells with BsAbs in the presence or absence of TFK-1 cells. hEx3-taFv showed higher production of IL-2 and IFN-γ compared with hEx3-Db especially in the presence of target cells (Fig. 4). The structural superiority of taFv format increases cytokine production of effector cells, resulting in its enhanced cancer growth inhibition effects.

Comparison of Growth Inhibition Effect of Each Multimeric hEx3—Recently, we reported the highly enhanced activity of a dimeric hEx3-Db (22). To evaluate the influence of the dimer-